Microstructure, mechanical properties, and fatigue performance of a PBF-LB Al2139ZrTi alloy

International Journal of Fatigue 202 (2026) 109245

Contents lists available at ScienceDirect

International Journal of Fatigue

journal homepage: www.elsevier.com/locate/ijfatigue

Microstructure, mechanical properties, and fatigue performance of a PBF-LB Al2139ZrTi alloy

Shawkat I. Shakil [a], Wiktor Bednarczyk [b], Marta Gajewska [c], Zaynab Mahbooba [d], Ankit Saharan [d], Andrea Tridello [e], Alessandro Benelli [f], Meysam Haghshenas [a,*]

[a] Fatigue, Fracture, and Failure Laboratory (F3L), Department of Mechanical, Industrial, and Manufacturing Engineering (MIME), University of Toledo, Toledo, OH 43606, USA
[b] Faculty of Metals Engineering and Computer Science, AGH University of Krakow, al. A. Mickiewicza 30, 30-059 Krakow, Poland
[c] Academic Centre for Materials and Nanotechnology, AGH University of Krakow, al. A. Mickiewicza 30, 30-059 Krakow, Poland
[d] EOS North America Inc., Pflugerville, TX 78660, USA
[e] Department of Mechanical and Aerospace Engineering, Politecnico di Torino, Turin, Italy
[f] Department of Applied Science and Technology, Politecnico di Torino, Turin, Italy

ARTICLE INFO

Keywords:
PBF-LB Al2139ZrTi
Microstructure
Tensile Properties
VHCF
Ultrasonic Fatigue

ABSTRACT

This study investigates the microstructure, tensile, and fatigue behavior of post-aged powder bed fused-laser beam (PBF-LB) Al2139ZrTi alloy, developed by EOS North America. The microstructure exhibits an equiaxed grain structure with an average grain size of approximately 1.5 μm and lacks any strong crystallographic texture. It also contains a dense dispersion of fine, uniformly distributed precipitates including: (i) $Al_3(Zr,Ti)$ dispersoids with $L1_2$-type structure, acting as semi-coherent nucleation sites that contribute to grain refinement; (ii) a unique $Al_3(Zr,Ti)$ plate-like phase, further confirming Zr–Ti-driven modification of precipitation pathways; (iii) Al(CuFeMn) and Al(MnCu) intermetallics, notably Al_7Cu_2 (Fe,Mn) and $Al_{20}Cu_2Mn_3$(T-phase), and (iv) Mg oxides, pointing to minor oxidation during processing. Notably, Al_2Cu-based θ′ and Ω phases are sparse, with only coarse θ-phase particles (~0.5–1 μm) at grain boundaries and fine plate-like Ω-phase (~tens of nm thick) along the [100] zone axis. Mechanical properties were evaluated via tensile testing, yielding ~ 470 MPa yield stress (YS), ~570 MPa ultimate tensile strength (UTS), and ~ 6.5 % elongation. Conventional (servo-hydraulic) and ultrasonic fatigue tests were performed to cover high cycle and very high cycle fatigue responses spanning up to 10^9 cycles. Fractographic analyses, including optical and electron microscopy techniques, were carried out to quantify the crack initiation mechanisms in the mentioned regimes.

1. Introduction

2XXX series aluminum alloys, such as Al2139, developed by the National Aeronautics and Space Administration (NASA) [1], are among the top choices for aerospace and defense applications due to their superior damage tolerance, high strength-to-weight ratio, excellent thermal conductivity, and corrosion resistance [2–5]. Despite these advantages, processing aluminum via laser-based additive manufacturing (AM) processes such as powder bed fusion–laser beam (PBF-LB) presents challenges due to its high laser reflectivity, rapid heat dissipation, solidification cracking, and oxidation sensitivity [6–8]. Hydrogen absorption, poor powder flowability, and gas-induced powder disruption further promote porosity, while the presence of a stable oxide layer on aluminum powder particles complicates fusion, acting as a barrier to complete melting and promoting defect nucleation [9,10]. Additionally, the high laser power needed to mitigate such issues risks the evaporation of key strengthening elements such as Mg and Zn, compromising the alloy's mechanical performance [11,12]. Nonetheless, advancements in process optimization, powder modification, and heat treatment strategies have enabled the successful fabrication of PBF-LB Al2139ZrTi with optimal properties.

Heat treatment is a critical post-processing step for PBF-LB Al2139ZrTi, governing the precipitation kinetics and resulting mechanical properties. In conventional 2XXX series aluminum alloys, a T8 temper, comprising solution treatment, cold working, and artificial aging, is often required to introduce dislocations that serve as nucleation sites for optimal strengthening precipitates [13,14]. This promotes a

* Corresponding author.
E-mail address: meysam.haghshenas@utoledo.edu (M. Haghshenas).

https://doi.org/10.1016/j.ijfatigue.2025.109245
Received 27 May 2025; Received in revised form 7 August 2025; Accepted 18 August 2025
Available online 20 August 2025

Nomenclature

AM	Additive Manufacturing
ASTM	American Society for Testing and Materials
BF	Bright Field
BSE	Backscattered Electron
cdf or $F_{Y\|x}$	Cumulative Distribution Function
DED	Directed Energy Deposition
DF	Dark Field
EBSD	Electron Backscatter Diffraction
EDS	Energy Dispersive Spectroscopy
FGA	Fine Granular Area
FCC	Face-centered cubic
HAADF	High-Angle Annular Dark Field
HCF	High Cycle Fatigue
HR-TEM	High-Resolution Transmission Electron Microscopy
IPF	Inverse Pole Figure
LoF	Lack of Fusion
MRD	Multiple of Random Distribution
NASA	National Aeronautics and Space Administration
PBF-LB	Powder Bed Fusion-Laser Beam
PSD	Particle Size Distribution
R	Stress Ratio ($\sigma_{min}/\sigma_{max}$)
SAED	Selected Area Electron Diffraction
SE	Secondary Electron
SEM	Scanning Electron Microscopy
SIF	Stress Intensity Factor
S-N	Stress Amplitude – Fatigue Life
TEM	Transmission Electron Microscopy
USF	Ultrasonic Fatigue
UTS	Ultimate Tensile Strength
VED	Volumetric Energy Density
VHCF	Very High Cycle Fatigue
XCT	X-ray Computed Tomography
YS	Yield Strength
σ_a	Stress Amplitude
σ'_f	Fatigue Strength Coefficient
b	Fatigue Strength Exponent
N_f	Number of Cycles to Failure
$\sqrt{area}$	Square Root of Projected Defect Area
K_d	Stress Intensity Factor of Killer Defect
S_a	Applied Stress Amplitude
μ_{X_l}	Mean of the Fatigue Limit Distribution,
σ_Y	Standard Deviations of the Fatigue Life
σ_{X_l}	Standard Deviations of the Fatigue Limit Distribution

high number density of small, dispersed precipitates by favoring nucleation over growth, leading to a more effective strengthening response. This is particularly important for alloys where the primary strengthening phase, such as θ' (Al_2Cu), has a high nucleation energy barrier, making homogeneous precipitation difficult. However, the presence of Mg and Ag in Al2139 alters this behavior by facilitating the formation of Mg-Ag co-clusters upon quenching, which act as preferential nucleation sites for the Ω-phase (Al_2Cu) on {111} planes, enabling peak strength to be achieved without mechanical deformation [15,16]. In the modified Al2139ZrTi alloy, the addition of Zr and Ti further refines precipitation kinetics. During rapid solidification in PBF-LB, a portion of Zr forms primary aluminides that promote grain refinement, while the remaining Zr and Ti remain in solid solution. Upon heat treatment, these elements precipitate as nanoscale Al_3(Zr,Ti) dispersoids, which serve as effective heterogeneous nucleation sites, altering the precipitation pathway [17,18]. This refined precipitation sequence, facilitated by rapid solidification and tailored heat treatment, enhances strength, stabilizes the microstructure, and reduces grain boundary precipitation, making Al2139ZrTi a promising candidate for high-performance applications.

In PBF-LB of high-strength aluminum alloys, the formation of coarse columnar grains is another challenge, which exacerbates hot tearing due to their restricted ability to accommodate thermally induced stresses [4,6]. A proven strategy to mitigate this issue is grain refinement, as equiaxed grains disrupt the continuity of thin liquid films during solidification and reduce local thermal gradients, thereby enhancing the material's resistance to cracking [3,19]. While Sc-based refiners can be used to refine grains in AM aluminum alloys [20,21], Zr and Ti additions have demonstrated similar effectiveness in grain refinement by forming Al_3(Zr,Ti) dispersoids, which act as potent nucleation sites in the melt pool [22,23]. This approach has been successfully applied in PBF-LB of Al-Cu-Mg alloys, significantly refining grain size and suppressing hot tearing [20,21]. In Al2139ZrTi, the in-situ formation of Al_3(Zr,Ti) dispersoids during rapid solidification refines the grain structure and enhances microstructural stability, making it a viable and cost-saving alternative to Sc-based grain refinement strategies.

Recent studies have advanced our understanding of the microstructural evolution and mechanical properties of AM Al2139 and its variants. Larini et al. [20] studied a Zr and Ti-modified Al2139 processed via PBF-LB, demonstrating that these elements refine the microstructure, eliminating hot cracking and promoting an equiaxed grain structure with grain sizes ranging from 300 to 600 nm at the melt pool boundaries and 800 nm to 2.0 μm at the center. A full transition from columnar to equiaxed grains was reported and attributed to the synergistic effect of Zr and Ti additions. An optimized T4 heat treatment increased the microhardness from 109.7 HV (as-built) to 186.1 HV, while prolonged thermal exposure led to overaging and solute (Cu and Mg) segregation, reducing hardness. Elambasseril et al. [24] investigated hot tearing and mechanical properties in PBF-LB Al2139, demonstrating that increasing the volumetric energy density (VED) above 1000 J/mm3 significantly reduced cracking but at the cost of Mg evaporation, which altered the alloy's strengthening response. The study further analyzed the effect of AlTiB grain refiners, which reduced hot tearing susceptibility by up to 6 % but did not fully transform the grain morphology into an equiaxed structure. The as-built material exhibited a predominantly columnar grain structure, while the introduction of AlTiB led to partial refinement, reducing grain size but not achieving a fully equiaxed microstructure. Mechanical testing revealed that the T6-treated PBF-LB Al2139 exhibited a yield stress of 350 MPa and an ultimate tensile strength (UTS) of 450 MPa, which, while comparable to cast counterparts, remained lower than wrought Al2139-T8 standards. Rees et al. [25] investigated hot cracking and porosity evolution in PBF-LB Al2139 with/without TiB_2 additions using in situ synchrotron X-ray imaging. TiB_2 reduced the volume fraction of hot cracks by up to 79 % at an optimized VED of 1250 J/mm^3, whereas at higher VEDs (5000 J/mm^3), the reduction was limited to 52 %. Crack propagation rates ranged from 76 to 110 mm/s, with cracks reaching lengths of 106–110 μm at the end of the melt track. Despite reducing cracking, TiB_2 additions increased porosity, particularly at high VEDs, due to oxide redistribution and gas entrapment near the melt track edges. Brice et al. [11,15] examined Al2139 fabricated via directed energy deposition (DED), providing valuable insights into precipitation behavior. Their work revealed that Mg evaporation during processing significantly reduced Ω-phase (Al_2Cu) formation, affecting mechanical performance. The peak-aged yield strength (321 MPa) and UTS (430 MPa) reported by Brice et al. [15] were comparatively low for Al2139 alloys produced, which was attributed to a lower number density of Ω-phase precipitates limiting the precipitation strengthening response. Brice et al. [11] further analyzed Mg loss during electron beam

DED, finding that up to 65 % of Mg evaporated, shifting precipitation toward the θ′-phase, which weakened the alloy. These findings highlight the critical role of composition control and process optimization in retaining alloying elements, influencing the mechanical performance of AM Al2139.

Despite the growing interest in AM Al2139, research on this alloy remains limited, with most existing studies focusing on mechanical properties (e.g., microhardness), while detailed microstructural evolution and fatigue behavior remain largely unexplored. Given the potential application of Al2139 in aerospace industries, where cyclic loading can lead to fatigue failure, a comprehensive understanding of its microstructure, defect characteristics, and mechanical behavior under static and cyclic loading (i.e., fatigue performance) is critical. Critical aspects such as grain morphology, defect distributions, precipitation behavior, and their influence on the mechanical and fatigue properties of Al2139 are largely unexplored. Therefore, this study aims to bridge these gaps by conducting the first detailed investigation on the microstructural evolution and the mechanical properties of Zr- and Ti-modified PBF-LB Al2139 alloy (i.e., Al2139ZrTi), covering quasi-static tensile performance as well as high cycle fatigue (HCF) and very high cycle fatigue (VHCF), i.e., beyond 10^7 cycles, response. Advanced microstructural characterization techniques, including scanning electron microscopy (SEM) and transmission electron microscopy (TEM), will provide insights into grain structure, size, morphology, and crystal structure of various precipitates, while X-ray computed tomography (XCT) will enable three-dimensional defect analysis and its influence on fatigue behavior. Additionally, SEM-based fractography analyses will identify critical defect types and their correlation with fatigue life, providing key insights into crack initiation, propagation, and fatigue failure mechanisms in PBF-LB Al2139ZrTi for the first time. By systematically linking microstructure, AM-caused defects, and fatigue performance (up to 10^9 cycles), this study aims to provide critical insights into the process-structure–property relationships of PBF-LB Al2139ZrTi, establishing foundational insights to optimize AM processing strategies for high-performance structural applications.

2. Materials and methods

2.1. Material processing and preparation

The material investigated in this study is EOS Aluminum Al2139 AM, or Al2139ZrTi, a high-strength Zr- and Ti-modified Al-Cu alloy developed by EOS North America, optimized for the PBF-LB process. The Al2139ZrTi powder with a particle size distribution (PSD) ranging from 20 to 63 μm is produced through gas atomization. The morphology of the Al2139ZrTi powder particles is illustrated in an SEM micrograph in Fig. 1. The image highlights the spherical nature of the particles, which contributes to optimal flowability and uniform layer deposition during the PBF-LB processing. The chemical composition of the powder is modified from *Aluminum Association Teal Sheet* specifications for Al2139 [26], with primary alloying elements including Cu, Mg, Ag, and Mn, along with trace metallic additions. The nominal and measured compositions of the EOS Al2139ZrTi alloy are listed in Table 1 [27]. The specimens were fabricated using an EOS M400-4 PBF-LB 3D printer. The printing process was carried out under an argon atmosphere with a build platform temperature of 175 °C to minimize residual stress. The printing process parameters are listed in Table 2. Following PBF-LB processing, all specimens underwent a post-aging heat treatment corresponding to the T4 condition. The heat treatment schedule included solution annealing at 490 °C for 45 min, followed by water quenching and natural aging for 72 h at room temperature (25 °C). The T4 condition was selected over artificial aging (e.g., T6) to preserve higher ductility while still achieving significant strength, providing a favorable strength–ductility balance. All tests and characterization were conducted on specimens in this heat-treated condition.

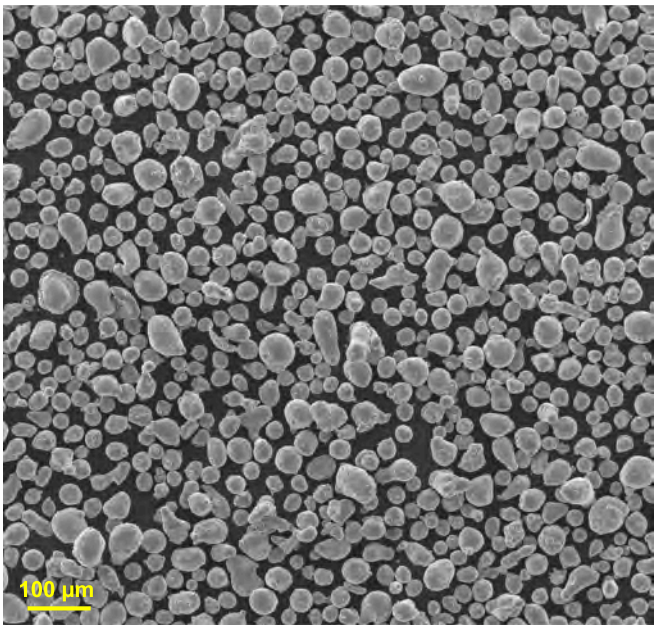

Fig. 1. SEM image of gas atomized EOS Aluminum Al2139ZrTi AM powder.

2.2. Microstructural characterization

Following PBF-LB processing and post-aging, samples of PBF-LB Al2139ZrTi were prepared for microstructural investigation using various metallographic procedures. The microstructural analysis was conducted using a multi-step methodology. Initial observations were performed using a digital autofocused microscope. Then, SEM and TEM were utilized for high-resolution imaging to quantify the size, shape, and morphology of the ultrafine grains and precipitates. The grain structure and texture were investigated through electron backscatter diffraction (EBSD) analysis, and the chemical composition of the fine precipitates was analyzed through TEM-based energy dispersive spectroscopy (EDS).

SEM imaging and EBSD analyses were performed using a Hitachi SU-70 field emission SEM equipped with a Bruker Quantax eFlashHD EBSD detector. Electrolytic polishing was conducted for EBSD sample preparation using a 30 % HNO_3 in methanol solution at −30 °C with an applied voltage of 20 V. Backscattered electron (BSE) imaging was carried out at an acceleration voltage of 10 kV, while EBSD data were collected at 25 kV. The EBSD maps covered areas of 320 × 240 μm with a step size of 250 nm for global analysis and 50 × 38 μm with a step size of 100 nm for detailed examination. Data processing and phase identification were conducted using Bruker Esprit 2.3 Software.

TEM analysis was carried out using an FEI Tecnai TF20 X-TWIN field emission gun microscope operating at 200 kV. Thin foils were prepared by grinding to ~ 100 μm thickness, followed by twin-jet electropolishing using a Struers TenuPol device in a 30 % HNO_3 methanol solution at −35 °C. High-resolution TEM (HR-TEM), dark field (DF) imaging, bright field (BF) imaging, selected area electron diffraction (SAED), and EDS were performed for detailed microstructural understanding.

X-ray computed tomography (XCT) analysis was carried out at the J-Tech@PoliTO laboratories to investigate the three-dimensional distribution of defects, as well as pore morphology and size variation, within the PBF-LB Al2139ZrTi samples. The scans were performed using a high-resolution tomography system equipped with a 300 kV X-ray source featuring a minimum focal spot size of 5 μm. During the scans, the specimen was positioned 40 mm from the source, while the detector was placed at 1500 mm, resulting in a spatial voxel resolution of approximately 5.3 μm. The system operated at a nominal power of 11.2 W, generated by applying 160 kV and 70 μA. A 200 μm-thick copper filter was employed to attenuate low-energy X-rays and enhance image

Table 1
Nominal and measured compositions (wt.%) of the EOS Al2139ZrTi alloy [27].

Element	Cu	Mg	Ag	Mn	Fe	Zr	Ti
Nominal	4.5–5.5	> 0.8	0.15–0.60	0.2–0.6	<0.15	Zr + Ti < 4.0	
Measured	5.47	1.59	0.57	0.49	0.08	1.00	0.90

Table 2
The PBF-LB process parameters for EOS Aluminum Al2139ZrTi.

Process parameter	Value
3D printer	EOS M400-4
Laser power	350–400 W
Laser speed	1000–1500 mm/s
Layer thickness	50 μm
Hatch distance	0.10–0.12 mm
Volume rate	4 × 5.0 mm^3/s
Minimum wall thickness	0.4 mm
Shielding gas	Argon
Build platform temperature	175 °C

contrast. Image acquisition was performed using a flat panel detector with a resolution of 2048 × 2048 pixels. Volumetric reconstruction of the scanned specimens was conducted using VG Studio software (VG MAX 3.5, Volume Graphics GmbH, Heidelberg, Germany), employing a filtered back projection algorithm. Defect identification and quantification were carried out using the integrated porosity analysis module, which applies contrast threshold-based image segmentation to accurately characterize the distribution and morphology of internal pores.

2.3. Quasi-static uniaxial tensile testing

Uniaxial tensile tests were conducted following the ASTM E8 standard [28] to extract the strength, Young's modulus, and elongation values of the studied material. A servo-hydraulic MTS system with 100 kN load capacity was employed to run the tensile tests. The tensile load was applied vertically (i.e., parallel to the build direction) at 10^{-3} s^{-1} of uniform strain rate. Following the tensile tests, the failed specimens were meticulously examined to understand their fracture mechanisms. The fractured surfaces were kept intact to preserve their original condition for analysis. This examination involved optical microscopy and SEM-based fractography utilizing an FEI Quanta 3D FEG SEM.

2.4. Conventional (servo-hydraulic) and ultrasonic fatigue testing

Conventional fatigue tests were conducted using an Instron servo-hydraulic test machine with a 100-kN load capacity. The tests followed the ASTM E466 standard [29], applying fully reversed (R = −1) load-controlled conditions at room temperature. A fixed testing frequency of 10 Hz was maintained. Before testing, all machined specimens were meticulously polished using silicon carbide sandpapers up to 7000 grit to achieve a mirror-finish, scratch-free surface. A sinusoidal waveform was applied, and testing continued until specimen failure or up to 5 million cycles, which was set as the runout threshold. Following the fatigue tests, fractographic analysis was conducted using a Keyence VHX-600 Digital Microscope and an FEI Quanta 3D FEG SEM to investigate crack initiation and propagation mechanisms.

Fatigue response beyond 10^7 cycles, VHCF regime, was assessed using a Shimadzu ultrasonic fatigue (USF) testing system (USF-2000A), operating at a loading frequency of 20 kHz to enable accelerated fatigue testing within a reasonable timeframe. The specimens were designed with an hourglass geometry tailored to Young's modulus (74 GPa) and density (2.84 g/cm^3) of the Al2139ZrTi alloy (specimen geometry and dimensions are provided in Fig. 2). To rule out the effect of surface roughness, all machined specimens were meticulously polished using silicon carbide sandpapers ranging from 3000 to 7000 grit. During testing, specimen temperature was monitored using an infrared laser thermometer, with a threshold of 40 °C to prevent thermal effects. To mitigate self-heating, compressed air was directed at the gauge region, and an intermittent driving sequence (pulse duration: 300 ms, pause: 200 ms) was implemented. The applied stress amplitude was determined based on tensile and conventional fatigue test results. Fatigue failure was detected through resonance frequency monitoring, with a frequency drop of 19.5 kHz, indicating specimen failure. Post-testing fractography was similarly carried out to analyze crack initiation and propagation mechanisms in the VHCF domain.

3. Results and discussion

3.1. Microstructure evolution in post-aged PBF-LB Al2139ZrTi

Fig. 3 presents large-area EBSD grain size maps from macroscopically distinct regions of the studied PBF-LB Al2139ZrTi alloy: a dense region (Fig. 3a) and a more porous region (Fig. 3b) viewed on the plane parallel to the build direction. These maps span multiple melt layers, capturing both interfacial zones and layer interiors. The average grain sizes (i.e., the arithmetic mean grain size, where each grain contributes equally regardless of its area) were 1.58 ± 0.80 μm and 1.71 ± 0.84 μm, respectively. Across all EBSD scans conducted, covering various regions and orientations, the average grain size consistently remained below 2 μm. Grains larger than 2.5 μm were rarely observed, and occasional grains approaching ~ 5 μm appeared randomly, without clustering in specific locations. These closely aligned values confirm a high degree of grain size uniformity across the build, regardless of porosity level or position.

Fig. 4 presents a representative EBSD-based view of the

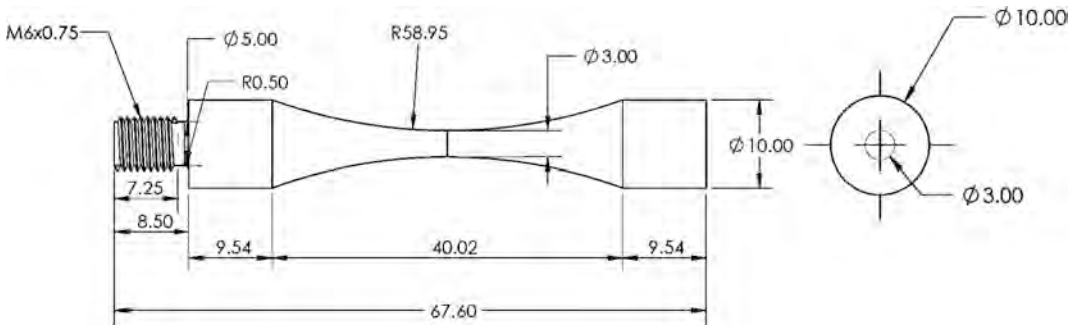

Fig. 2. Hourglass specimen geometry and dimensions for USF testing of Al2139ZrTi. All dimensions are in mm.

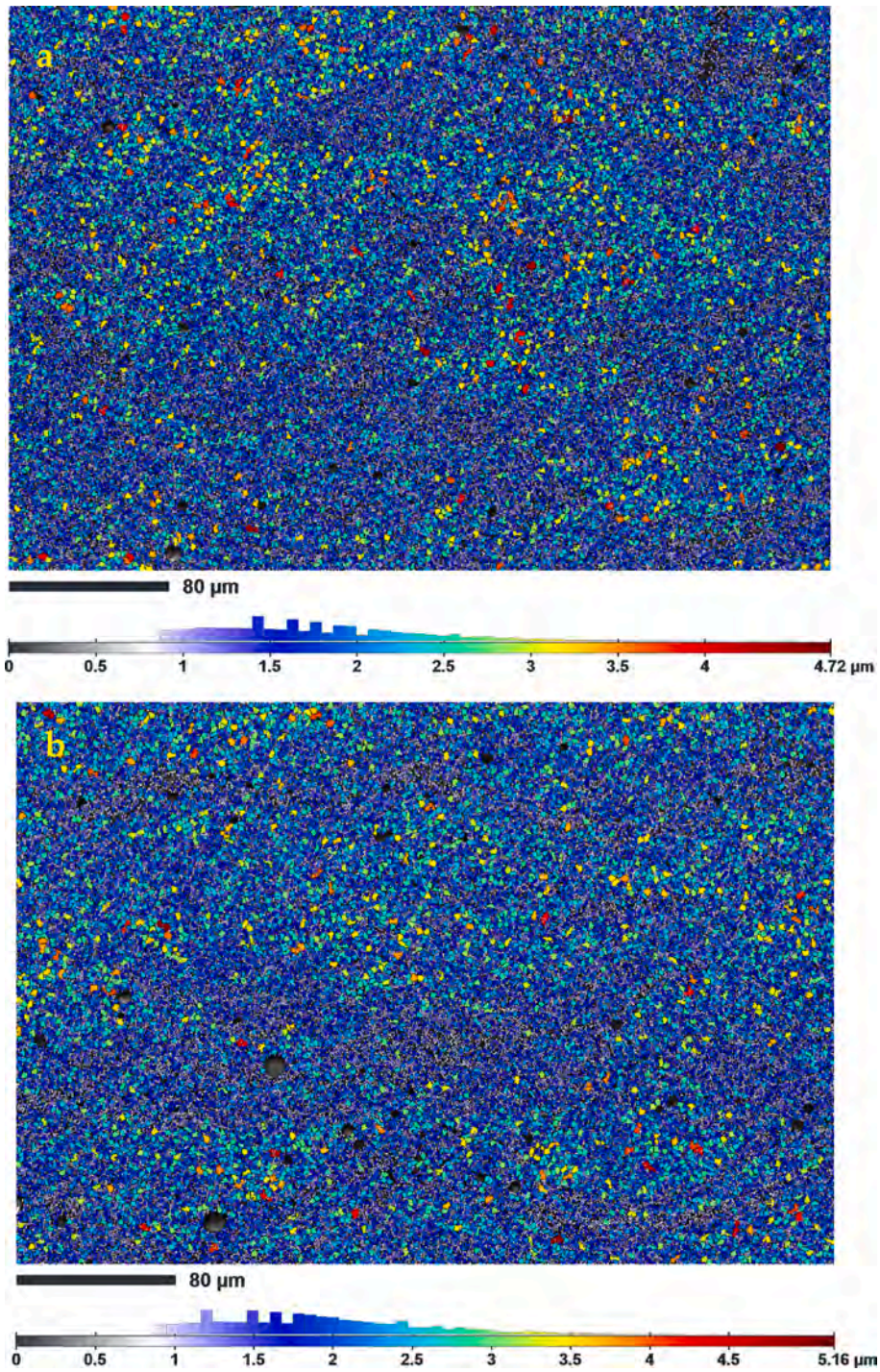

Fig. 3. Large-scale EBSD grain size maps acquired from macroscopically distinct regions of the studied PBF-LB Al2139ZrTi alloy on a plane parallel to the build direction: (a) a dense region (average grain size: 1.58 ± 0.80 µm); (b) a porous region (average grain size: 1.71 ± 0.74 µm).

microstructure, highlighting grain morphology, crystallographic orientation, and texture across orthogonal planes. The reference cube in the figure illustrates the spatial orientation: the Z-axis corresponds to the build direction, while the X- and Y-axes define the scanning plane during laser exposure. Based on this, the XY plane represents the horizontal plane parallel to the build plate, and the XZ plane represents a vertical cross-section along the build direction. The inverse pole figure (IPF) maps of the XY plane (Fig. 4a) and XZ plane (Fig. 4b) both reveal a uniform, equiaxed grain morphology. The average grain size measured on the XY plane is 1.53 ± 0.61 µm, and on the XZ plane is 1.68 ± 0.62 µm. No evidence of columnar grains is observed, even in the XZ plane aligned with the build direction, indicating a complete columnar-to-equiaxed transition, a feature attributed to the grain refinement effect of Zr and Ti, which promotes the formation of Al_3(Zr,Ti) dispersoids during solidification. Another plausible explanation for the observed refined and uniformly equiaxed grain structure and weak crystallographic texture is recrystallization during the post-aging heat treatment. The solution treatment temperature used in this study exceeds the typical recrystallization temperature of aluminum, and the elevated dislocation density and residual stresses introduced by the PBF-LB process can further lower this threshold.

Crystallographic orientation analysis using the (111) pole figure

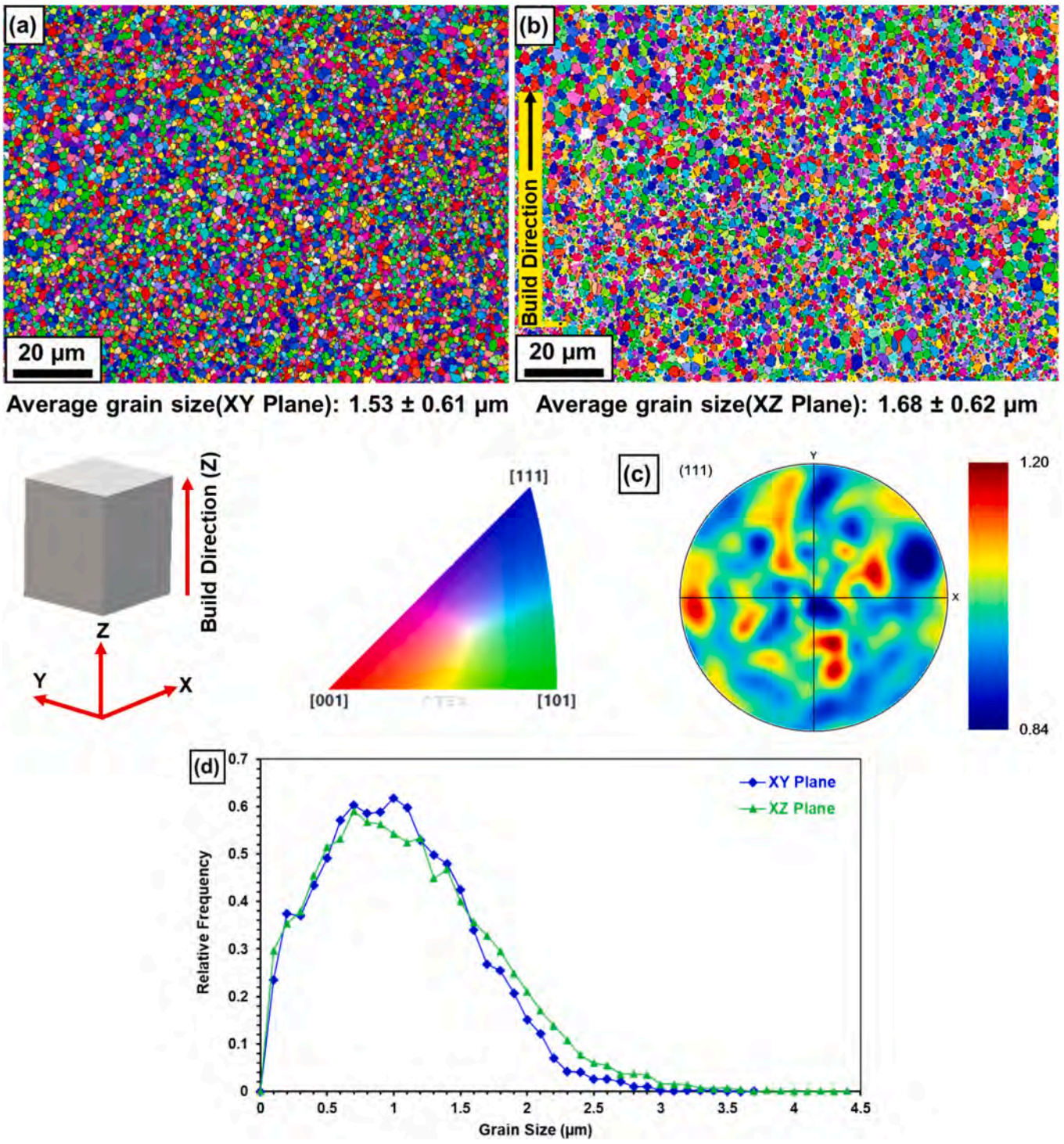

Fig. 4. EBSD analysis confirmed uniform grain size in both horizontal and vertical directions, regardless of location within the layers, on post-aged PBF-LB Al2139ZrTi: (a) IPF map of the XY plane; (b) IPF map of the XZ plane showing equiaxed morphology; (c) (111) pole figure from the XZ plane confirming weak crystallographic texture; (d) grain size distribution plots for XY and XZ planes with most grains falling between 0.5 and 2.0 μm.

(Fig. 4c) reveals a weak and diffuse texture in the XZ plane, indicative of the absence of strong preferential alignment of the crystals. This is confirmed by the low multiples of random distribution (MRD) values observed on the pole figure scale, confirming the near-random crystallographic orientation. Such minimal texture suggests a low degree of anisotropy, which is beneficial for structural applications where isotropic mechanical behavior is desired. The grain size distribution extracted from EBSD is shown in Fig. 4d, comparing the grain size profiles in the XY and XZ planes. Both planes exhibit nearly indistinguishable grain-size distributions (Fig. 4d), consistent with the average values reported above (average grain size of 1.53 ± 0.61 μm on the XY plane and 1.68 ± 0.62 μm on the XZ plane) and confirming uniform refinement with negligible anisotropy. Therefore, the EBSD results demonstrate that the combination of rapid solidification in PBF-LB and post-aging heat treatment in Al2139ZrTi produces a stable, uniformly equiaxed microstructure with refined grains, weak texture, and minimal directional dependence.

The TEM microstructure observed in the studied PBF-LB Al2139ZrTi

alloy indicates a distinct precipitation behavior, diverging from conventional Al-Cu-Mg-Ag alloys. Fig. 5 presents a detailed TEM characterization of the alloy, illustrating both bright field (BF) and high-angle annular dark field (HAADF) microstructures, alongside corresponding EDS elemental maps in the lower panels, revealing a dense dispersion of fine, uniformly distributed precipitates with compositional variations. The identified precipitates include: (i) $Al_3(Zr,Ti)$ dispersoids – these fine, semi-coherent or coherent precipitates, equiaxed shaped with $L1_2$-type structure, form due to the presence of Zr and Ti, acting as potent nucleation sites and contributing to grain refinement; (ii) elongated or plate-like $Al_3(Zr,Ti)$ precipitates – also exhibiting an $L1_2$-type structure, these particles are likely a distinct morphological variant formed under different local Zr/Ti ratios (elongated particles generally displayed a higher local Zr/Ti ratio compared to the equiaxed ones); (iii) Al (CuFeMn) and Al(MnCu) precipitates – these appear to be present in significant fractions, but at the same time are evenly distributed, forming as intermetallic phases that can impact mechanical performance; phases like $Al_7Cu_2(Fe,Mn)$ (I_4/mcm) and $Al_{20}Cu_2Mn_3$ (*T* phase) where detected in the microstructure; while Al_7Cu_2Fe precipitates are typically coarse, Mn substitution tends to cause their refinement, which may enhance the strength and ductility by reducing stress concentrations and crack initiation sites. On the other hand, ***T*** phase, while not belonging to primary strengthening phases, may contribute to strength enhancement indirectly through supporting dimensional stability and microstructural control; (iv) Mg oxides, indicating possible oxidation during processing. Notably, the expected Al_2Cu (Ω and θ′ phases) are not prominent in the microstructure. Nevertheless, a small amount of coarse spherical θ-phase precipitates (500 nm to 1 μm) located at grain boundaries, as well as fine plate-like Ω-phase precipitates (a few tens of nanometers thick), were observed. This suggests that the addition of Zr and Ti alters the precipitation dynamics, possibly by competing for available Cu and Mg, leading to an increased formation of $Al_3(Zr,Ti)$ at the expense of conventional Al_2Cu-based strengthening phases.

This deviation in precipitation behavior stems from thermodynamic and kinetic factors, including: (i) any influence on the nucleation barrier for Al_2Cu in the presence of Zr and Ti, which may delay or suppress its formation; (ii) solute competition and preferential precipitation of $Al_3(Zr,Ti)$, consuming solute elements and limiting the availability of Cu and Mg for θ′/Ω-phase nucleation; (iii) solidification dynamics of PBF-LB, which could impact solute segregation and precipitate evolution during subsequent heat-treatment [30–32]. Further insights into the precipitate characteristics are provided by TEM analysis in Fig. 6, which captures the morphologies of individual precipitates along with crystallographic identification details through selected area electron diffraction (SAED) patterns. The $Al_3(Zr,Ti)$ dispersoids (Fig. 6a), consistently observed along the [110] zone axis with an $L1_2$-type structure at varying magnifications, underscore their role as stable, nanoscale features that likely enhance high-temperature strength and creep resistance by pinning grain boundaries [33–35]. A thin plate-shaped $Al_3(Zr,Ti)$ precipitate is also shown in Fig. 6b with a consistent

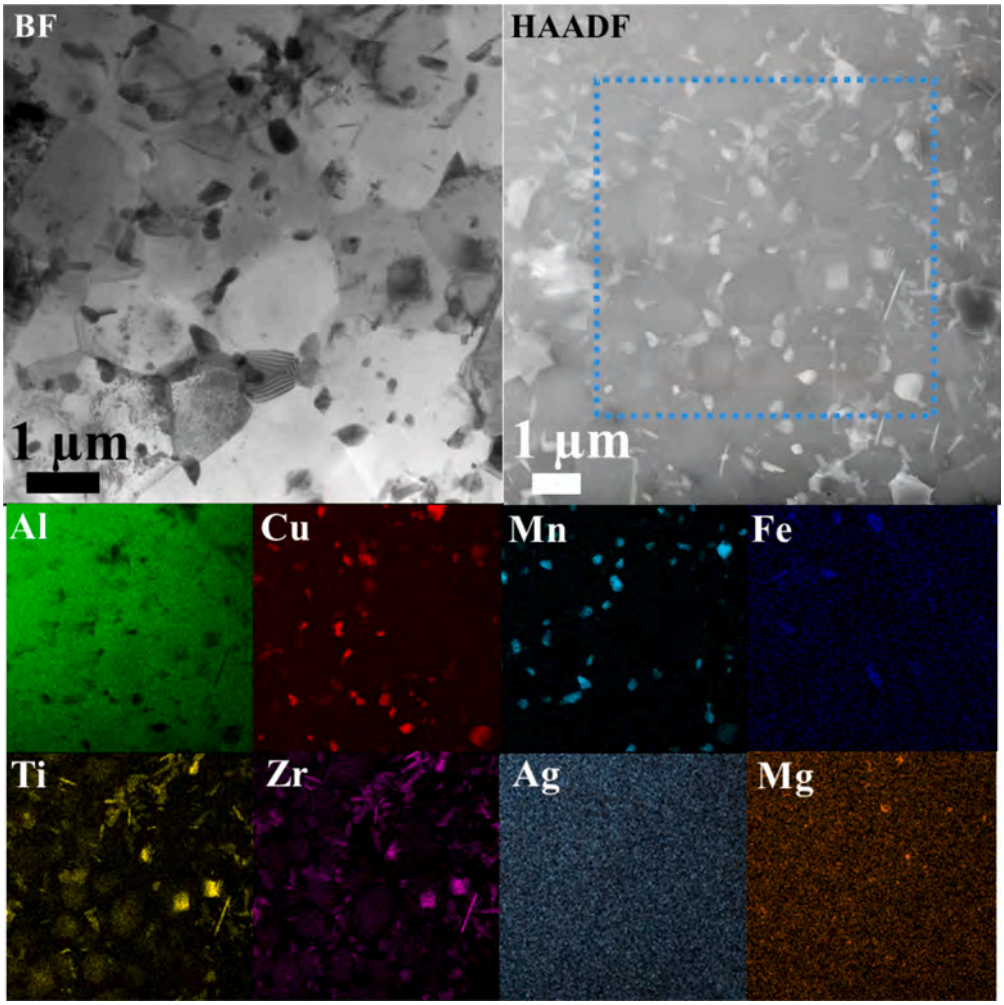

Fig. 5. TEM microstructure of the PBF-LB Al2139ZrTi alloy along with corresponding EDS elemental maps. The bright field (BF) and HAADF images (top) show a dense distribution of precipitates. The dashed rectangle in the HAADF image indicates the region analyzed in the EDS maps (bottom), which reveal compositionally distinct precipitate phases.

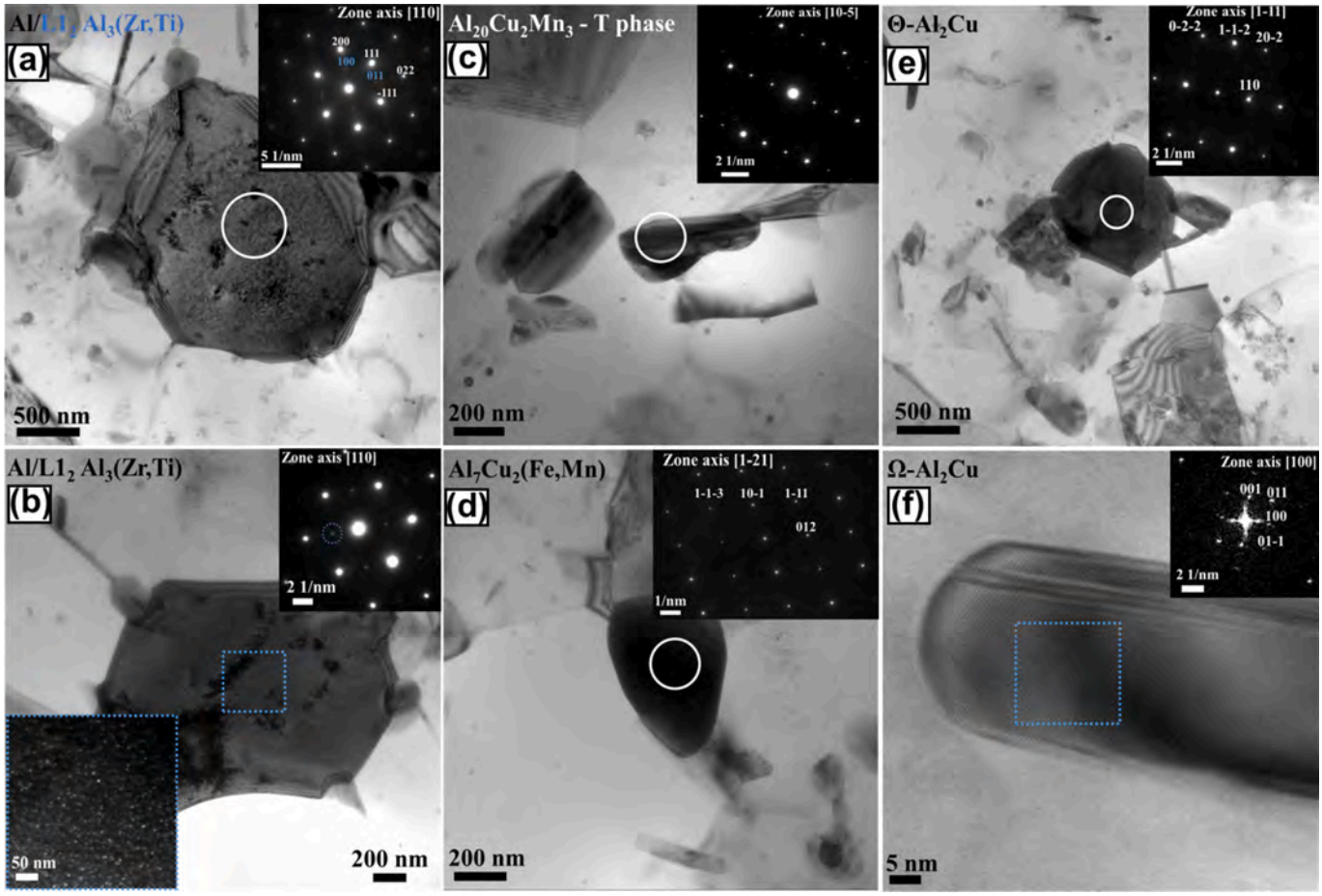

Fig. 6. TEM images of individual precipitates in the Al2139ZrTi alloy, showcasing their distinct morphologies and corresponding SAED patterns (insets): (a) L12-Al3(Zr,Ti)-dispersoid (coarser), (b) L12-Al3(Zr,Ti)-thin plate (finer), (c) $Al_{20}Cu_2Mn_3$ (T-phase), (d) Al_7Cu_2 (Fe,Mn), (e) Al_2Cu (θ' phase, globular), and (f) Al_2Cu (Ω phase, thin-plate).

$L1_2$ structure confirmed by SAED. The distinct crystallographic orientations of intermetallic phases like $Al_{20}Cu_2Mn_3$(T-phase) along $[10\bar{5}]$ and Al_7Cu_2 (Fe,Mn) along $[1\bar{2}1]$ (see Fig. 6c & d) suggest a heterogeneous precipitation sequence, where Mn-driven refinement in the latter could improve toughness by dispersing stress concentrations, while the presence of T-phase hints at a stabilizing effect on the microstructure during thermal cycling. The less frequent, sparse Al_2Cu phases, with coarse θ-phase at grain boundaries along $[1\bar{1}1]$ and fine plate-like Ω-phase along [100] are presented in Fig. 6e & f. Their less frequent occurrence is an indication of suppressed formation of such conventional strengthening phases; the absence of such phases may shift the alloy's strengthening mechanism toward dispersoid-dominated hardening, potentially at the cost of reduced ductility. These observations highlight how Zr and Ti additions, combined with the rapid solidification of PBF-LB, orchestrate a complex interplay of phases, offering opportunities to tailor mechanical properties for purpose-specific applications through precise control of different precipitate systems and their distribution.

Based on elemental distribution maps and STEM-HAADF images, size distributions and number densities of individual precipitate types in the studied alloy were quantitatively analyzed. As illustrated in Fig. 7, the precipitates were classified into three categories based on their composition: those containing Zr and Ti (Al_3(Zr,Ti)), those containing Cu but no Fe or Mn (Al_2Cu-based Ω and θ′), and intermetallics containing Mn and/or Fe. To quantitatively assess these precipitates, the equivalent diameter (D_{eq}) was calculated using the Worthley formula [36]; i.e., $D_{eq} = \frac{2D_{max} \times D_{min}}{D_{max} + D_{min}}$. The number density of the particles in unit area N_A was calculated using $N_A = \frac{N}{A}$, where N is the number of particles, and A is the total analyzed area. The number density of particles per unit volume N_V was determined based on $N_V = \frac{N_A}{t + \overline{D}}$, where N_A is the number density in unit area, t is the thickness of the thin foil and $\overline{D}$ is the arithmetical mean equivalent diameter of the particles. The resulting statistical parameters for each precipitate type are summarized in Table 3.

Among these, Al_3(Zr,Ti) precipitates, often exhibiting elongated or plate-like morphology, were the most abundant, with the highest number density of approximately 4.8 μm^{-3} and a relatively small mean diameter of 132 ± 91 nm. The size distribution in Fig. 7a clearly shows that the material is dominated by a fine fraction of precipitates (50–125 nm), which results from post-production heat treatment. These particles were homogeneously distributed throughout the aluminum matrix. Their small size and high density make them particularly effective at hindering dislocation motion and suppressing subgrain coarsening. However, larger particles (e.g., above 300 nm), which likely formed during the production stage as primary precipitates, were also present. Nonetheless, the relatively low number of these primary particles, and consequently their influence on the mechanical properties, is significantly lower compared to the fine secondary precipitates. In contrast, θ′/Ω precipitates exhibited a much lower number density (1.28 μm^{-3}) but a significantly larger average diameter of 310 ± 172 nm, as well as the broadest size distribution (as shown in Fig. 7b), with individual precipitates reaching sizes of up to approximately 1.1 μm. The lower number density and larger size of these precipitates suggest that they play a significantly smaller role in material strengthening than Al_3(Zr, Ti) dispersoids. Mn/Fe-rich particles (Fig. 7c) were also observed less frequently compared to Al_3(Zr,Ti), with a number density of 1.32 μm^{-3}

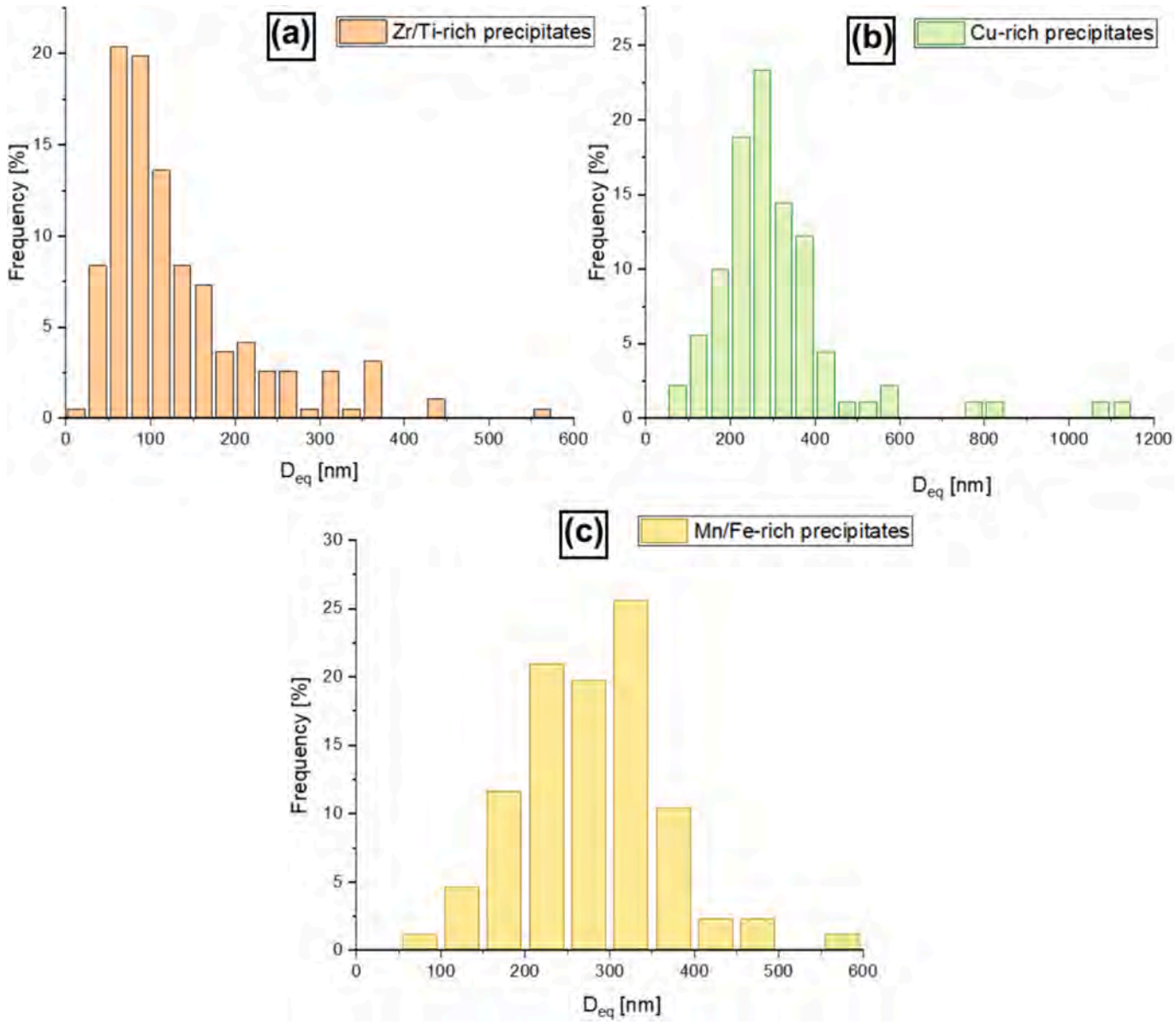

Fig. 7. Size distribution histograms of precipitates in the Al2139ZrTi alloy, classified by composition based on EDS mapping: (a) Zr/Ti-rich $Al_3(Zr,Ti)$ dispersoids, (b) Cu-rich precipitates (Al_2Cu, Ω/θ′), and (c) Mn/Fe-rich intermetallics.

Table 3
Quantitative summary of precipitate statistics in the Al2139ZrTi alloy.

Parameter	Zr/Ti-rich precipitates	Cu-rich precipitates	Mn-rich precipitates
Total analyzed area A [μm^2]	171.43	171.43	171.43
Area fraction A_A [%]	2.24	5.18	3.37
Number density N_A [μm^{-2}]	1.11	0.52	0.50
D_{eq} range [nm]	20–550	67–1140	86–585
Mean diameter $\overline{D}_{eq}$ [nm]	132 ± 91	310 ± 172	279 ± 86
Number density per unit volume N_v [μm^{-3}]	4.8	1.28	1.32

and an average size of 279 ± 86 nm. These precipitates, often located at grain boundaries, may not contribute significantly to strength directly, but they can influence grain boundary pinning and potentially affect recrystallization behavior.

3.2. Volumetric defect inspection

A detailed defect analysis was carried out on two machined samples, i.e., the F25 specimen (with the geometry of the specimens subjected to conventional fatigue (F) tests) and the U21 specimen (with the geometry of the specimens subjected to ultrasonic (U) fatigue tests). The 3D spatial distributions of the pores are shown in Fig. 8. In the F25 specimen, the largest defect exhibits an irregular and tortuous morphology (see Fig. 8a), whereas the largest pore in U21 is more spherical and compact (see Fig. 8b). This trend is quantitatively confirmed in Fig. 8c, which shows the sphericity plotted against the characteristic defect size. The U21 sample shows consistently higher sphericity, especially for larger pores, whereas the F25 sample is characterized by a larger number of irregular and elongated pores. This difference may be attributed to the different specimen geometry [37] and is also verified by analyzing the defects at the origin of the fatigue failures carried out in Sections 3.4 and 3.5. Additionally, spatial variation on the build plate could also affect defect formation, as the gas flow is not 100 % uniform across the entire build plate.

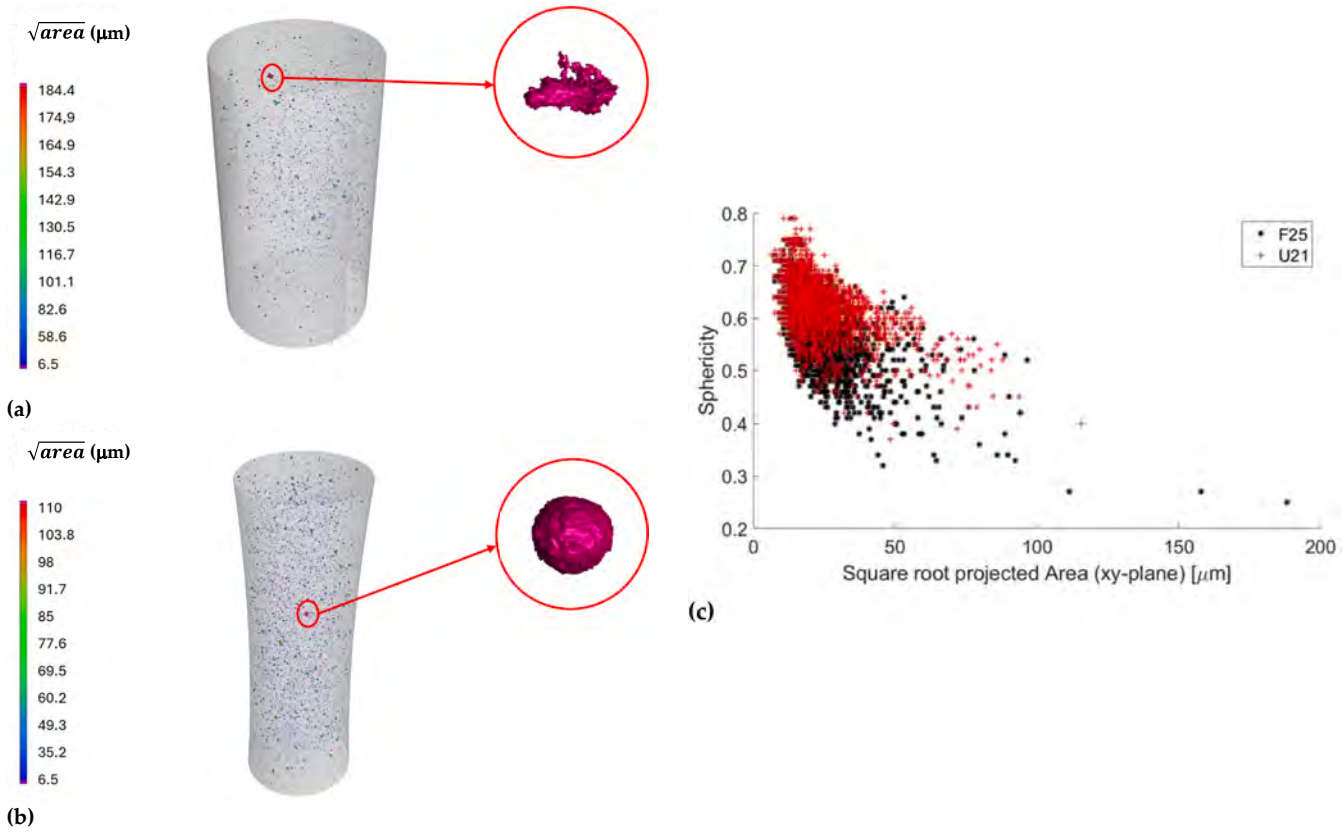

Fig. 8. 3D visualizations of pore distributions in (a) F25 and (b) U21 samples, highlighting the largest defect based on the square root of the projected area perpendicular to the loading direction (zoomed-in views); (c) Sphericity as a function of projected area (in the XY plane) for pores in F25 and U21 samples.

The main geometrical and volumetric characteristics of the specimens are summarized in Table 4, which were directly extracted from the VG Studio Max software, using the porosity analysis module. In the following, the square root of the area of the defect projected in a plane perpendicular to the specimen axis, i.e., the loading direction, has been considered. Indeed, this size is the one controlling the fatigue response, according to [38,39].

Despite both samples exhibiting high relative density, indicating low total porosity, differences are observed in defect size distribution and morphology. The pore count histogram (Fig. 9) shows that in both samples, most pores fall within the 10–30 μm range. Compared to U21, the F25 specimen displays a more uniform distribution across the 10–40 μm range, whereas U21 shows a sharp peak at 10–20 μm followed by a steep decline. This suggests that in the U21 sample, smaller defects are present, while F25 is characterized by a wider range of defect sizes, though still predominantly small. The difference may be correlated to the sample geometry. While F25 presents a constant diameter of 5 mm, the U21 specimen features an hourglass profile with a reduced central diameter of 3 mm.

Table 4
Summary of geometrical and porosity parameters for samples F25 and U21 from XCT analysis.

Parameter	F25	U21
Inspected Volume (mm^3)	201	78.50
Porosity volume (mm^3)	0.04	0.06
Relative density	0.9998	0.9993
Average equivalent diameter (μm)	20.05	16.13
Maximum equivalent diameter (μm)	117.74	116.99

3.3. Quasi-static tensile properties

Fig. 10a shows the tensile flow curve of the studied post-aged PBF-LB Al2139ZrTi alloy, tested in the build direction (vertically). The material exhibits a yield plateau with a 0.2 % offset yield stress (YS) of 468.05 ± 2.90 MPa, a UTS of 573.35 ± 2.06 MPa, and a total elongation of 6.47 ± 0.16 %, along with a modulus of elasticity of 74.29 ± 0.46 GPa. These mechanical properties are closely tied to the alloy's tailored microstructure. The refined, equiaxed grains (less than 2 μm in size) produced by the combined effects of PBF-LB rapid solidification and $Al_3(Zr,Ti)$ dispersoid formation contribute to grain boundary strengthening and isotropic deformation, as supported by the weak crystallographic texture observed in EBSD analyses. TEM results further reveal that the strengthening response is dominated not by conventional Al_2Cu (Ω/θ') precipitates, which are only sparsely observed, but by a dense network of $Al_3(Zr,Ti)$ dispersoids and secondary intermetallics present in significant quantities, such as Al(CuFeMn) and ***T***-phase ($Al_{20}Cu_2Mn_3$). These features, especially the $L1_2$-structured dispersoids, serve as effective obstacles to dislocation motion and enhance dimensional stability under stress. However, the suppressed precipitation of fine Ω and θ' phases, likely due to solute competition and altered nucleation pathways induced by Zr and Ti, may limit the full potential for precipitation hardening. The moderate ductility observed can thus be attributed to a microstructure governed by dispersoid-dominated hardening, with additional influences from residual porosity/defects, solute segregation, and the presence of intermetallic phases.

To contextualize these properties, Fig. 10b compares the mechanical performance of Al2139ZrTi with other Al–Cu–Mg alloys of similar composition. The comparison includes: (i) a Zr-modified alloy Al-Cu-Mg alloy fabricated by PBF-LB (Zhang et al. [40]), (ii) a Ti-modified Al-Cu-Mg alloy processed via PBF-LB (Zhang et al. [41]), and (iii) a naturally aged (T4 aged) wrought AA2519 (Al-5.64Cu-0.33Mn-0.23 Mg-0.15Zr-

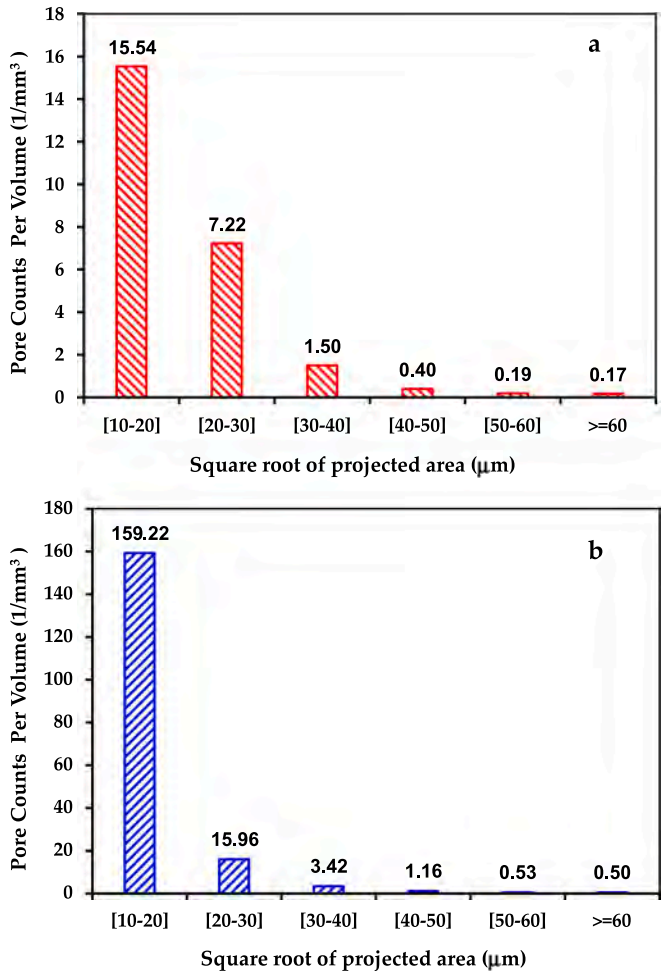

Fig. 9. Pore size distributions expressed as pore counts per volume for (a) the F25 sample and (b) the U21 sample (XY plane).

0.11Ti) alloy (Zuiko et al. [42]). The PBF-LB processed Al–Cu–Mg/Zr alloy reported by Zhang et al. [40] in the as-built condition exhibited YS of 446 MPa and UTS of 451 MPa, but limited ductility (2.67 %), suggesting poor strain accommodation due to the absence of post-processing. On the other hand, the Ti-modified alloy studied by Zhang et al. [41], also tested in the as-built state, displayed much lower strength (YS = 293.2 MPa, UTS = 426.4 MPa) but greater elongation (~9.1 %), indicative of a softer, more compliant microstructure with reduced internal stress and absence of aging. In these studies, Al_3Zr and Al_3Ti particles, respectively, were found to be the major nucleating and growth-limiting agents, which significantly aided microstructural refinement and reduced process-induced cracks/defects compared to the unmodified Al-Mg-Zr alloys [40,41]. The wrought AA2519 alloy under T4 temper (natural aging), used as a benchmark for aerospace-grade Al–Cu–Mg systems, demonstrated UTS of 455 MPa and elongation of 18.4 % [42]. While this alloy offers excellent ductility, it lags in strength performance, showing ~ 35 % lower YS and ~ 21 % lower UTS than the PBF-LB Al2139ZrTi developed in this work. Collectively, these comparisons confirm that the naturally aged PBF-LB Al2139ZrTi alloy achieves a highly competitive strength–ductility synergy among both additively manufactured and wrought Al–Cu–Mg–(Zr,Ti) alloys. This superior performance stems from its tailored microstructure, featuring ultra-fine equiaxed grains, high-density $Al_3(Zr,Ti)$ dispersoids, and moderate presence of T-phase and secondary intermetallics, alongside suppressed θ'/Ω precipitation and low residual porosity. The outcome is a stable, dispersion-strengthened microstructure with consistent deformation behavior and low expected anisotropy making the alloy suitable for applications demanding a balance between strength, stability, and manufacturability.

The fracture surfaces of the tensile-tested specimens T1 and T2 were thoroughly analyzed via fractography based on secondary electron (SE) imaging under SEM, as illustrated in Fig. 11. Specimen T1, characterized by slightly higher elongation, exhibits distinct fracture morphology (Fig. 11a). The central area of Fig. 11a (blue rectangle) reveals a typical ductile fracture characterized by abundant and uniformly distributed micro-voids or dimples, indicating significant plastic deformation before fracture. Conversely, the peripheral region near the specimen surface (orange rectangle) presents a notably flatter fracture morphology with no dimples. Fig. 11b provides a comprehensive fractographic overview of specimen T2, which demonstrated slightly lower elongation during tensile testing. The fracture surface prominently features a large lack of fusion (LoF) defect near the edge of the specimen, as shown in the enlarged red-rectangle region. Upon further magnification of the fracture surface (green rectangle), features consistent with un-melted particles become apparent. These features are notably finer than typical feedstock particles and lack the three-dimensional morphology associated with partially fused powder. Instead, they appear as poorly wetted regions embedded within the lack of fusion (LoF) zone, supporting the interpretation that they are remnants of insufficient melting. This justifies the use of the term 'LoF defect' and directly correlates with reduced ductility. High magnification views of additional regions reveal diverse microstructural features: the blue box highlights well-developed dimple patterns characteristic of ductile fracture, while the violet box zooms further into a void area containing fine agglomerates that may be un-melted. These fractographic observations underline the detrimental impact of manufacturing defects, particularly LoF containing un-melted particles and wetting, on the mechanical integrity and ductility of additively manufactured materials.

3.4. Conventional fatigue behavior and fractographic analysis

The conventional fatigue response of the PBF-LB Al2139ZrTi alloy is presented in Fig. 12, with testing performed under fully reversed loading (R = –1) in the build direction. The S-N data (i.e., stress amplitude (σ_a) versus the number of cycles to failure (N_f)) in Fig. 12a demonstrate typical scatter, and the arrows indicate runout specimens that did not fail within 5 million cycles (fatigue strength of approximately 94 MPa at 5 million cycles). The fatigue data reported for other PBF-LB Al-Cu-Mg alloys, such as Ti-modified PBF-LB Al2024 [43] and TiB_2-modified PBF-LB Al-Cu-Mg-Ag [44], exhibited comparable fatigue performance. A Basquin-type power law fit, $\sigma_a = \sigma'_f (2N_f)^b$ [45], was applied to the data excluding runouts (Fig. 12b), yielding a fatigue strength coefficient (σ_f) of 1846.3 MPa and an exponent (b) of 0.208, with a correlation coefficient R^2 = 0.84. These results confirm a robust fit and highlight the predictable fatigue performance of the alloy even when failure is driven by process-induced defect variability.

While there is no available fatigue data for the exact composition used in this study (Zr- and Ti-modified Al2139), the literature on Al-Cu-Mg-Ag alloys provides fatigue data for both conventional and additively manufactured conditions, offering insight into how processing methods, post-processing, and surface treatments influence fatigue life. Kermanidis et al. [46] reported fatigue strength for laser beam welded Al-Cu-Mg-Ag (AA2139) alloy in T8 and T3 temper. No significant difference between the two tempers was observed, particularly at stress levels below 150 MPa. A fatigue strength of 115 MPa at 10^7 cycles was reported for both conditions. Köckritz et al [47] studied PBF-LB AA2139 under multiaxial loading, comparing as-built and surface-treated conditions, and found no significant improvement in fatigue life from surface treatment due to incomplete removal of process-induced defects like voids and undercuts, with failure often initiating from large subsurface defects and resulting in comparable S-N curves. Gazizov et al. [48] studied the effect of peak-aged T6 and thermomechanically

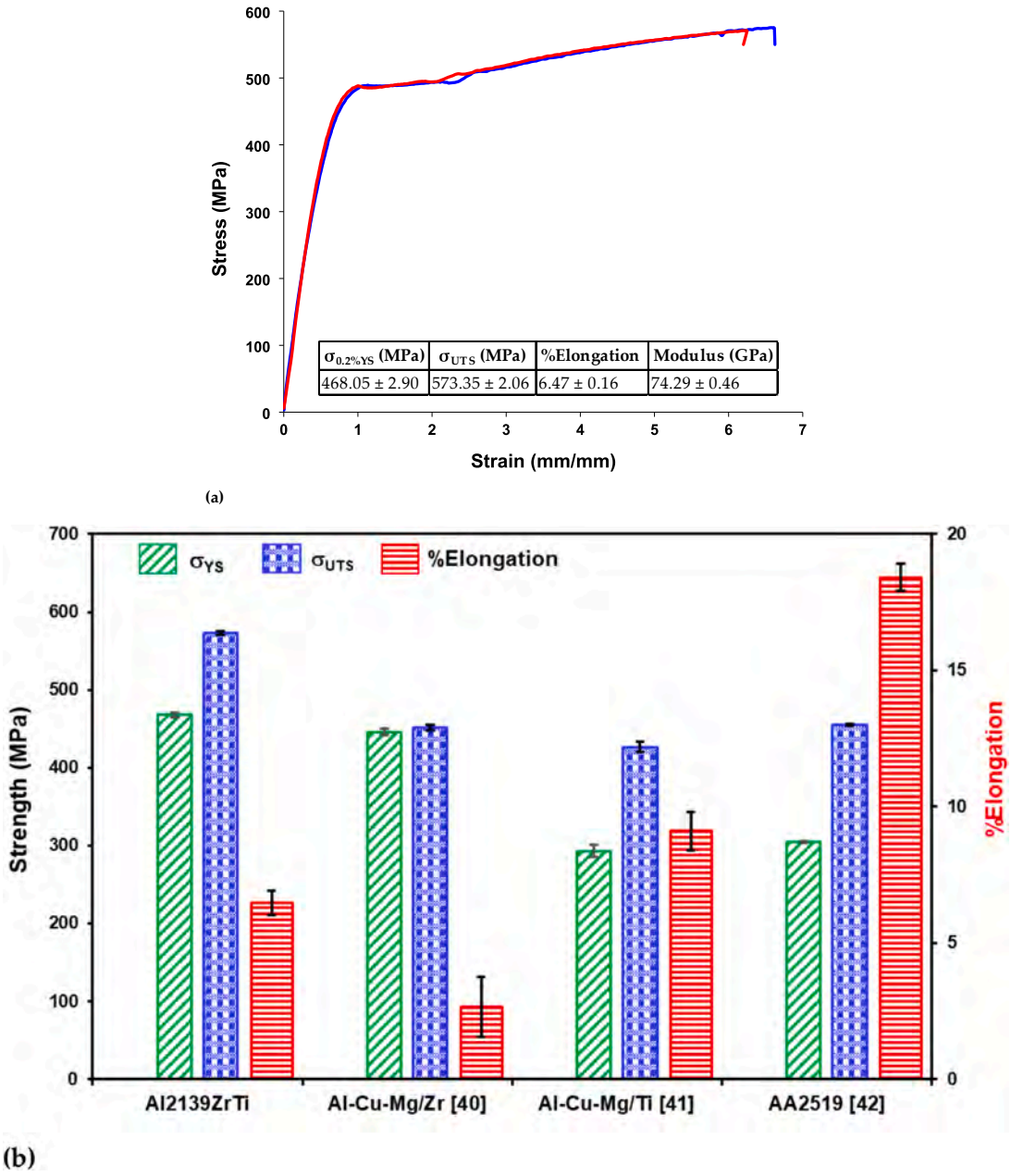

Fig. 10. (a) Uniaxial tensile stress–strain curves of post-aged PBF-LB Al2139ZrTi (tested in the build direction) and (b) comparison of tensile properties with similar alloy composition from the literature [40–42].

processed T840 tempers (the latter involving 40 % cold rolling followed by aging) on wrought AA2139, under a load ratio of R = 0.1. The T840 condition exhibited superior fatigue performance, which was attributed to a refined microstructure and the presence of shearable precipitates that promote transgranular fracture and reduce crack propagation rates. Djugum et al. [49] studied fatigue resistance in underaged (UA) conditions for wrought Al-Cu-Mg alloy AA2001 (similar base to AA2139 but without Ag) at R = 0, finding enhanced fatigue life in UA compared to fully hardened T6 temper despite lower yield stress (270 MPa UA *vs* 396 MPa T6), linked to dynamic precipitation and self-healing mechanisms during cycling that delay crack initiation and reduce crack randomness.

To understand failure origins and mechanisms, detailed fractography analyses were performed on specimens that failed at various fatigue lives. Based on the comprehensive fractographic investigation of the alloy, a complex landscape of crack initiation scenarios was found, closely governed by defect type, size, location, and interaction with the specimen surface. Across the specimens examined, failures predominantly initiated from large-sized LoF defects, which are often found to be irregularly shaped, sharp-edged features with high local stress concentration potential. These LoF defects, initiating the fatigue crack, were frequently discovered near the surface or were fully surface-connected, highlighting the significant role of defect accessibility in fatigue crack nucleation. In several cases, un-melted particles were found embedded within the large LoF regions, compounding stress localization and promoting early failure. Multiple crack initiation behavior was also prevalent, particularly in specimens with more than one surface-connected defect or with complex defect clusters near the periphery. Furthermore, chemical analysis using EDS showed the presence of oxides (mostly based on Mg_2O) in the crack initiation zones.

Fig. 13 highlights the fracture surfaces of two specimens (F11 and F16), imaged under secondary electron mode, where fracture initiation was linked to LoF defects. In Fig. 13a, specimen F11 (187 MPa, 1.45×10^5 cycles) failed from two distinct initiation sites, both located along the periphery of the specimen and directly connected to the surface. The

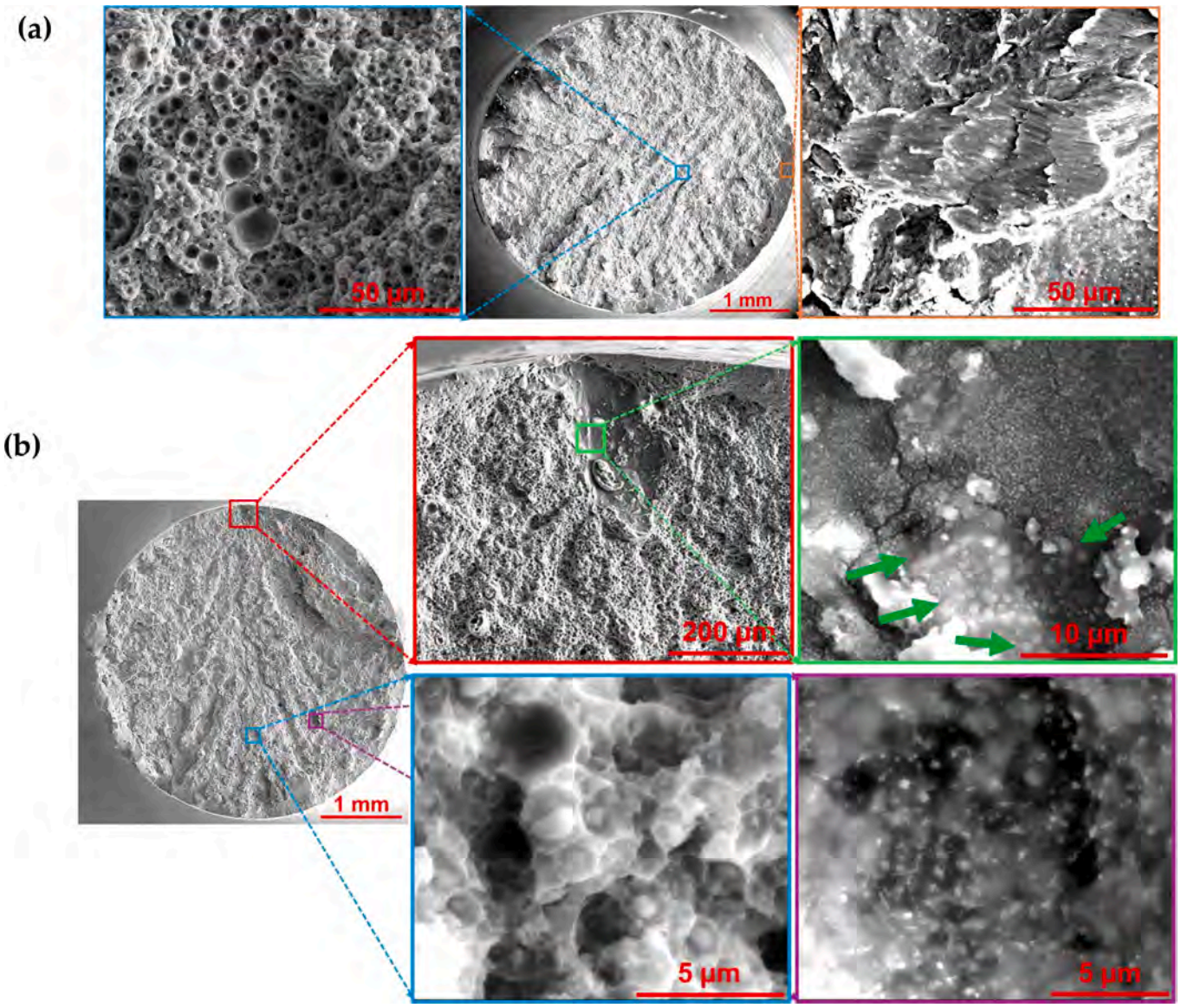

Fig. 11. SEM fractography of tensile fracture surfaces: (a) specimen T1 with central region having ductile dimples (blue box) and peripheral flat regions indicating brittle behavior (orange box); (b) specimen T2 featuring significant lack-of-fusion defects influencing ductility along with un-melted particles and dimples.

positions of these flaws with distinct propagation marks suggest bidirectional fatigue crack initiation, each creating its propagation zone. In Fig. 13b, specimen F16 (234 MPa, 2.15×10^4 cycles) failed from a large, triangular LoF defect measuring 172 µm in size (i.e., $\sqrt{area}$ of the defect) and located only 3.8 µm away from the surface (i.e., the distance from the surface to the edge/boundary of the defect). A nearby smaller LoF defect is also visible in Fig. 13b, which did not have a distinct propagation zone of its own, indicating that the geometry/size/orientation of the dominant feature was decisive in crack nucleation and driving the crack propagation. In both cases, the fracture surfaces exhibit classic fatigue features (e.g., the initiation zone followed by a stable propagation zone with propagation ridges, a dimpled rupture zone, and secondary porosity all over the surface.

Fig. 14 presents another, more subtle failure scenario observed in specimen F17 (281 MPa, 3.47×10^4 cycles), which exhibited dual initiation sites. The upper initiation site (highlighted by a red border) was dominant, as evidenced by a wide propagation area extending across the fracture surface. A secondary initiation point, located at the bottom (blue border), generated a smaller yet well-developed propagation zone.

EDS mapping from both sites revealed notable enrichment of magnesium and oxygen, strong indicators of oxide film formation at the initiation points. These oxides, likely formed during laser processing or due to trapped surface contamination, act as brittle inclusions, lowering the threshold for crack initiation and providing weak interfaces for early decohesion. While the EDS signal for other elements (e.g., Al, Cu, Ag, Mn, Zr, and Ti) remained homogeneously distributed, these oxide films were localized in the initiation zone and might have played an important role in fatigue damage. Fig. 15 further features specimen F20 (328 MPa, 3.83×10^3 cycles), which failed from a large LoF defect embedded with un-melted powder and oxide-covered particles. The fracture origin displays a dense, brittle morphology, with spherical features coated in magnesium-rich oxides and clustered satellite particles along the interfacial boundary (marked with blue arrows on the bottom right images in Fig. 15). These inclusions not only introduce local stiffness mismatches but also interrupt metallurgical bonding, exacerbating interfacial stress and promoting micro-void formation. The position of the defect was slightly deeper (151 µm from the surface), but its complex internal structure made it an ideal crack nucleation site under elevated cyclic stress.

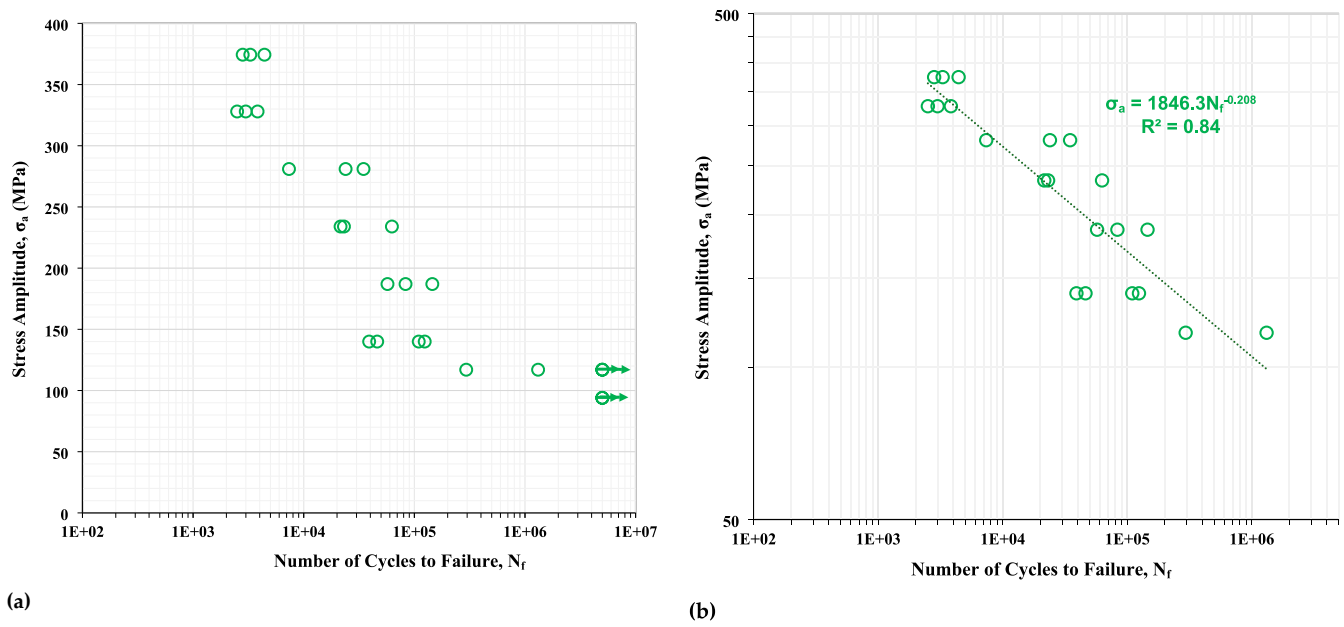

Fig. 12. (a) S-N data obtained from conventional servo-hydraulic fatigue testing of PBF-LB Al2139ZrTi alloy under fully reversed loading (R = –1), with green arrows indicating runout specimens; (b) Basquin fit excluding runouts.

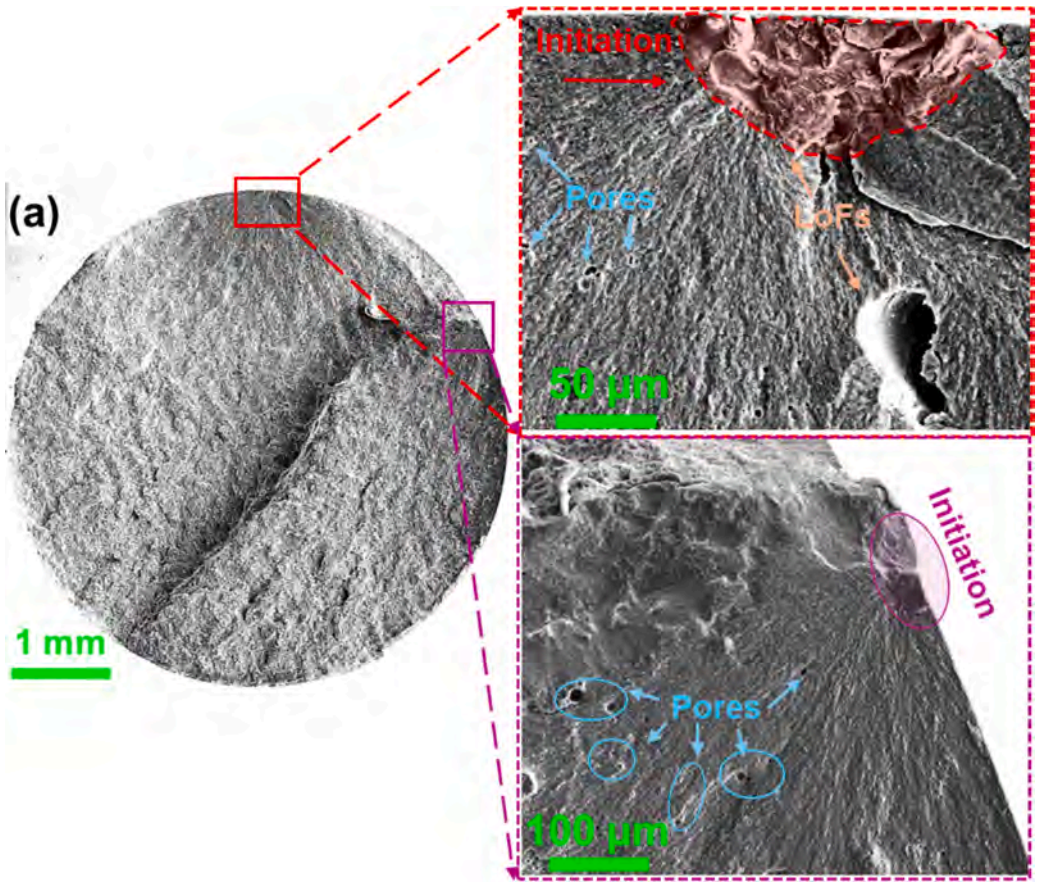

Fig. 13. (a) Fracture surface of specimen F11 (187 MPa, 1.45 × 10^5 cycles), showing crack initiation from multiple sites; (b) Specimen F16 (234 MPa, 2.15 × 10^4 cycles) failed from a large triangular LoF defect; additional smaller LoF visible left of the critical defect.

The trends observed across these and additional specimens (see Table 5 for a comprehensive summary of fractographic measurements) demonstrate that fatigue life in the studied PBF-LB Al2139ZrTi alloy is strongly influenced by the size and surface proximity of the defects. To isolate the effect of defects, meaningful comparisons can be made among specimens tested at the same stress level. At 140 MPa, for example,

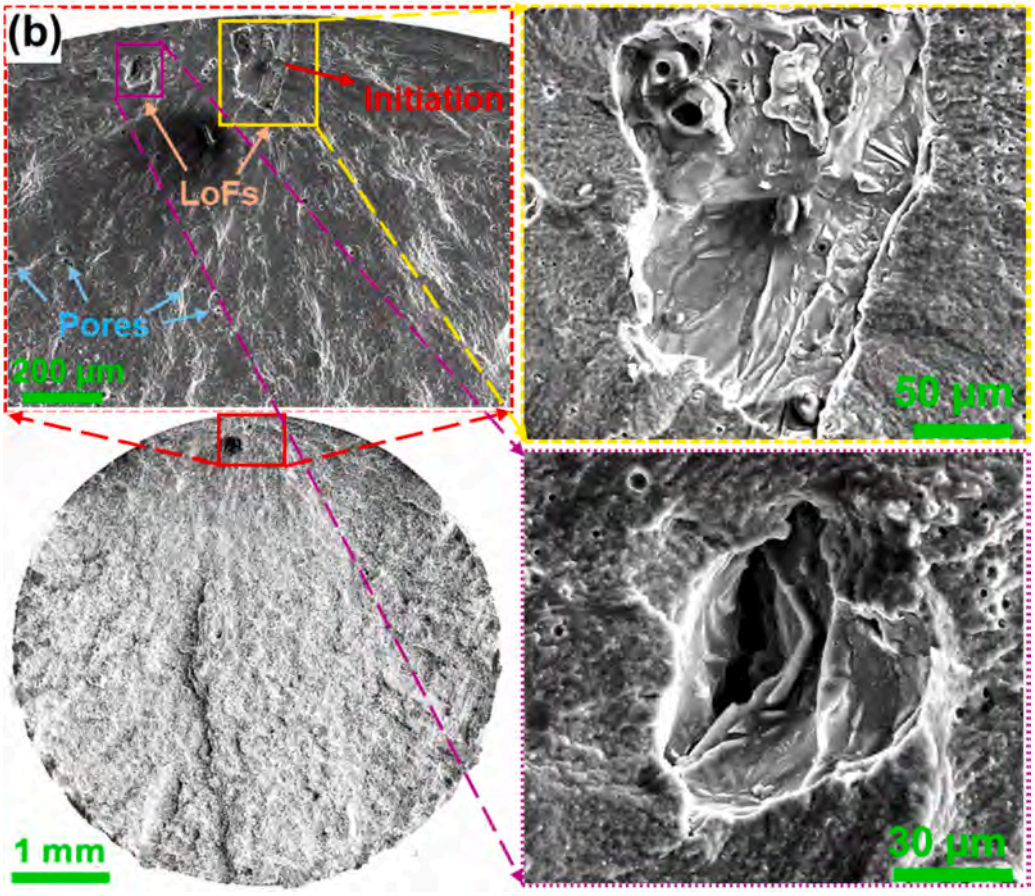

Fig. 13. (*continued*).

specimen F7 survived 1.24×10^5 cycles with a 130 μm surface-connected defect, while specimen F10, containing a much larger 312 μm defect located just 3.8 μm below the surface, failed much earlier at 3.90×10^4 cycles. Similarly, at 234 MPa, specimen F14 (64 μm defect) lasted 6.27×10^4 cycles, whereas F15 (86 μm) and F16 (172 μm) failed earlier, at 2.31×10^4 and 2.15×10^4 cycles, respectively. While F16 had a significantly larger defect, its relatively shallow depth (3.83 μm from the surface) helped delay failure slightly compared to F15, emphasizing that not only defect size but also its precise distance from the surface critically governs fatigue life under identical loading. Internal or sub-surface defects can also be detrimental but typically result in longer lives than equivalent-sized surface-attached flaws. For example, specimen F19, which contained a 183 μm internal defect located 108 μm from the surface, failed at 7.36×10^3 cycles under 281 MPa, similar to or slightly longer than surface-connected defects at the same stress level (e.g., F23: 239 μm defect at 946 μm depth, 4.42×10^3 cycles; F24: 90 μm surface defect, 3.29×10^3 cycles). This reinforces that defect accessibility to the surface critically governs crack nucleation.

3.5. Very high cycle fatigue (VHCF) behavior and fractographic analysis

The VHCF behavior of the studied PBF-LB Al2139ZrTi alloy is presented in Fig. 16. The VHCF S-N data are plotted in Fig. 16a, covering fatigue lifetimes extending up to 10^9 cycles. Like conventional fatigue data, the VHCF results exhibit variability. Runout specimens, indicated by arrows at 10^9 cycles, show that failure no longer occurs at stress amplitudes around 105 MPa. A Basquin fit applied to failure data (excluding runouts) yielded a fatigue strength coefficient (σ_f) of 694.11 MPa and a fatigue strength exponent (b) of −0.087 ($R^2 = 0.89$), as shown in Fig. 16b. Compared to conventional fatigue, the lower slope here reflects the transition to crack initiation-dominated failure, where the majority of the fatigue life is consumed in the microstructural neighborhood of a flaw before long-range crack propagation.

To explain the failure mechanisms in the VHCF regime, a detailed fractographic assessment was performed on all fractured specimens (U5 to U12), revealing two major classes of crack origins: spherical gas pores and irregular LoF defects. Both defect types were seen to trigger failures either with or without the formation of a fisheye, a distinct fracture morphology characterized by a quasi-circular crack front at its center, which is often surrounded by a fine granular area (FGA) formation. The formation of the fisheye pattern depended primarily on the spatial location of the critical defect rather than its type. While both LoF defects and spherical pores originated fatigue cracks, only defects located deep within the bulk promoted the fisheye pattern, where the surrounding matrix impedes early crack growth and delays initiation. The surface-adjacent flaws consistently led to direct crack propagation without fisheye formation. These observations suggest that internal shielding delays crack nucleation, facilitating the development of a fisheye zone characteristic of VHCF behavior.

In Fig. 17, two contrasting fracture behaviors are presented for specimens that failed from LoF defects. Specimen U5 (126 MPa, 3.28×10^8 cycles) failed from an LoF defect located just 39 μm away from the surface. The initiation site features a complex, irregular defect morphology accompanied by un-melted particles (green box), wetted region (light blue box), and local oxide formation, as confirmed by EDS maps showing distinct Mg- and O-rich regions at the crack-initiating LoF site, with other elements homogeneously distributed. No fisheye morphology was observed in Fig. 17a, and the crack propagated directly from the exposed defect. The absence of a transition zone or fine granular area underscores that surface accessibility dominated the crack nucleation process, with limited confinement by the surrounding

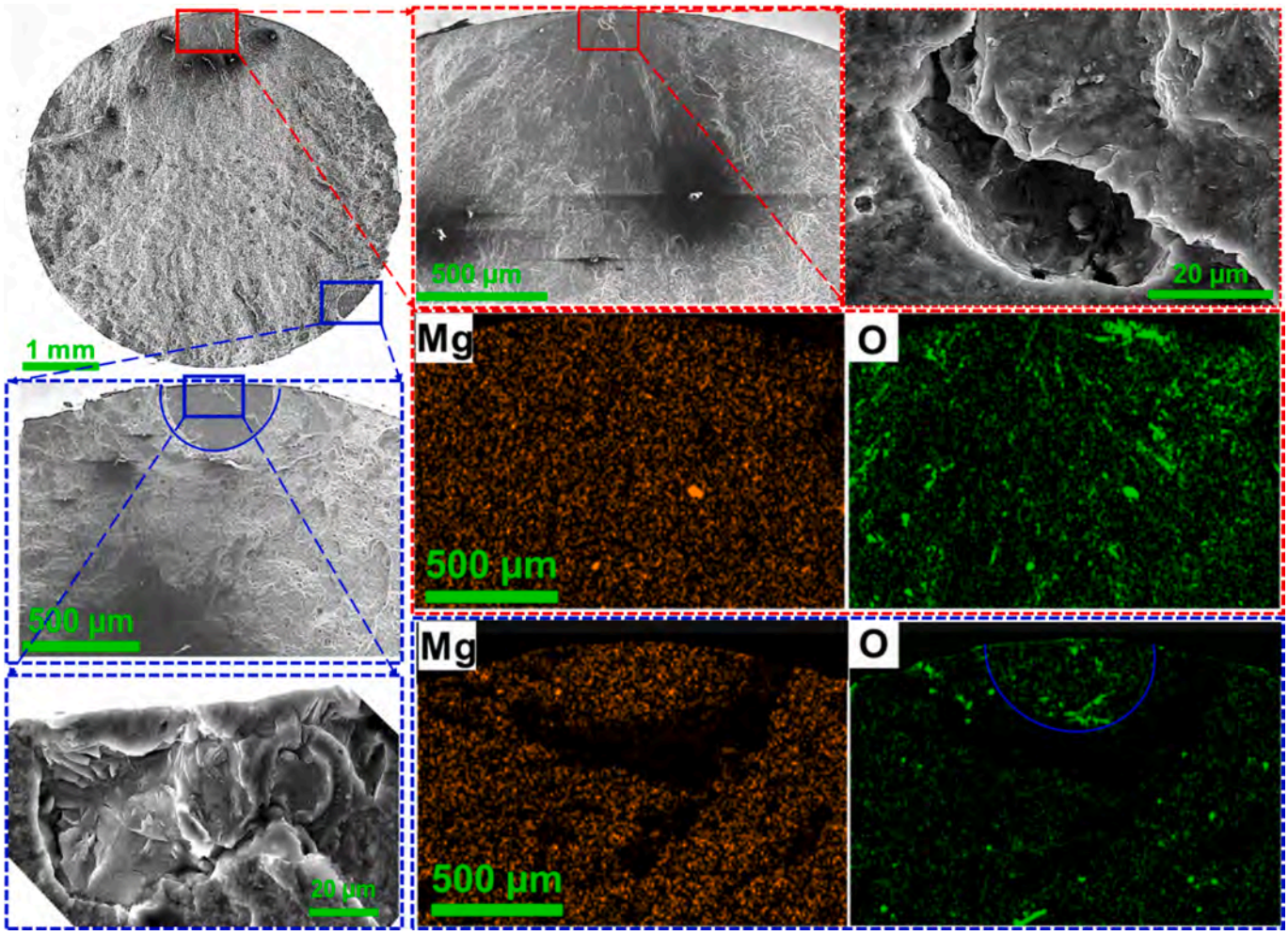

Fig. 14. Fracture surface of specimen F17 (281 MPa, 3.47 × 10^4 cycles) showing dual crack initiation: primary site (top, red) with dominant growth, and secondary site (bottom, blue); EDS detected Mg-based oxides.

microstructure that could have delayed crack growth. In contrast, specimen U7 (136 MPa, 1.93 × 10^8 cycles) failed from an LoF defect located ~ 549 µm below the surface. The fracture surface displayed a distinct fisheye bounded by a transition zone and enclosing a fine granular area at the origin. The fully embedded, irregular defect allowed for prolonged crack incubation, consistent with internal-defect-driven VHCF behavior commonly observed in AM aluminum alloys [50,51].

Fig. 18 presents fracture surfaces associated with spherical pore-initiated cracks. Specimen U8 (136 MPa, 1.83 × 10^8 cycles) failed from a spherical pore measuring ~ 71 µm, positioned only ~ 10 µm from the surface. The fracture surface is devoid of fisheye morphology; the pore is nearly surface-attached, and the crack propagated radially outward with no intermediate crack-arresting (see Fig. 18a). Specimen U9 (145 MPa, 1.05 × 10^8 cycles), on the other hand, illustrates classic VHCF failure behavior from an internal spherical pore located ~ 197 µm beneath the surface. The pore, although smaller (~71 µm), was deeply embedded, allowing sufficient time for crack incubation. A well-defined fisheye with a sharp boundary is visible in Fig. 18b, indicating a prolonged initiation period before unstable crack growth.

These comparative analyses confirm that both the size of a defect and its spatial position relative to the surface influence fracture behavior in VHCF, but their contributions differ in how they affect crack initiation and propagation. While larger defects inherently act as stronger stress concentrators and have been traditionally associated with reduced fatigue life [52], investigations, both in the conventional [53] and VHCF regime [54], also emphasize the role of defect location as a dominant factor. In the current study, as summarized in Table 6, deeply embedded defects (e.g., U6, U7, U10, and U12, all > 400 µm from the surface) exhibited well-developed fisheye morphologies and longer incubation phases, despite variation in defect size. Conversely, specimens with smaller but near-surface defects (e.g., U5, U8, and U11, < 50 µm depth) failed earlier and without fisheye formation, indicating that surface accessibility accelerates crack initiation irrespective of size. These findings are in line with the foundational work of Murakami et al. [52] and, more recently, by Tusher et al. [50]. While Romano et al. [55] examined HCF behavior in AM AlSi10Mg, their fracture mechanics modeling supports this trend, showing that surface-connected defects exhibit higher effective stress intensity factors than internal ones of equal size. Thus, while defect size contributes to the local crack driving force, proximity to the surface governs whether a defect becomes critical under VHCF, particularly through its influence on incubation delay and fisheye formation. These insights emphasize the need to simultaneously minimize both defect size and surface connectivity to enhance the VHCF performance of the PBF-LB Al2139ZrTi alloy.

3.6. Statistical analysis and modeling of fatigue life

The aim of the analyses carried out in this Section is to verify the statistical distribution of fatigue life in the whole HCF-VHCF life range, based on the extensive experimental activity described in previous Sections. The experimental data obtained through conventional and ultrasonic tests have been analyzed separately. For the conventional

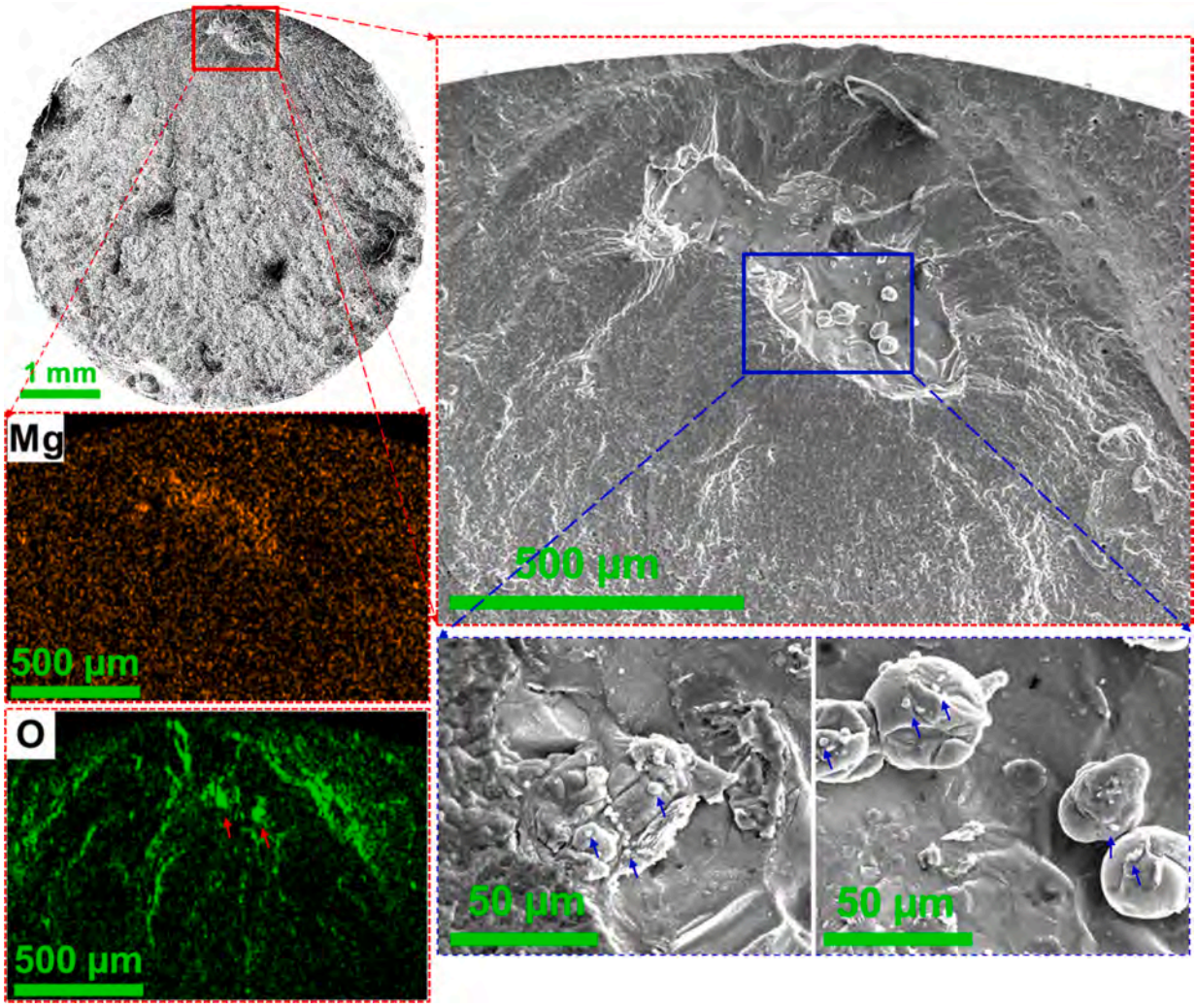

Fig. 15. Fracture surface of specimen F20 (328 MPa, 3.83 × 10^3 cycles) showing a large LoF defect with un-melted particles. EDS maps reveal ~ 20 µm spherical, oxide-coated particles, with satellite particles visible at high magnification.

tests, a model with a monotonic decreasing trend and a fatigue limit has been considered. The cumulative distribution function (*cdf*), $F_{Y|x}$, of the logarithm of the fatigue life random variable, $Y = \log_{10}(N_f)$, being N_f the number of cycles to failure is reported in Eq. (1):

$$F_{Y|x} = \Phi\left(\frac{y-(a+b\bullet x)}{\sigma_Y}\right)\Phi\left(\frac{x-\mu_{X_l}}{\sigma_{X_l}}\right) \quad (1)$$

being x the logarithm of the applied stress amplitude, s_a, $\Phi(\bullet)$ the *cdf* of a standardized normal distribution, a and b constant coefficients modeling the linear decreasing trend in the finite life region, μ_{X_l} the mean of the fatigue limit distribution, σ_Y and σ_{X_l} the standard deviations of the fatigue life and the fatigue limit distributions, respectively. The parameter estimation has been carried out by applying the Maximum Likelihood Principle, i.e., failures and runout data are therefore both considered. It must be noted that this model is capable of discerning if an asymptotic trend is present. Indeed, if the data do not show a clear fatigue limit, the estimated μ_{X_l} parameter tends to zero. For the ultrasonic fatigue tests, the model in Eq. (1) has also been employed. The lognormal distribution has been used in this analysis for its versatility and fitting capabilities. Other distributions may be used, like the Weibull distribution, and they are expected to provide similar results. Moreover, it must be noted that this analysis does not aim to discriminate between the type of defects at the origin of the fatigue failure (i.e., LoF defects or gas porosities), since the characteristic defect size, rather than its origin, affects the fatigue response. Accordingly, a distribution for the fatigue life accounting for the different defect types has not been considered. Fig. 19 plots the experimental data (obtained through conventional and ultrasonic fatigue tests) on an S-N plot, together with the estimated 0.1, median, and 0.9-th S-N curves.

According to Fig. 19, the experimental data from the conventional fatigue tests display a decreasing trend followed by an asymptote, indicating that the model in Eq. (1) is appropriate for fitting the data. The estimated median fatigue limit is 116 MPa. Experimental variability is greater in the finite life regime but decreases as it approaches the fatigue limit. This can be attributed to the concentration of runout data at only two stress amplitudes, two at 117 MPa and two at 94 MPa, which may reduce the apparent scatter in this life region. For the ultrasonic fatigue tests, the same trend has been estimated, with the median fatigue limit being equal to 116.5 MPa. For this data, on the other hand, the variability is quite constant within the investigated fatigue life range. It is interesting to note that the fatigue limit estimated with the conventional and ultrasonic fatigue tests is very close, even if the tests are stopped at 5 × 10^6 cycles for the former and at 10^9 cycles for the latter. Similarly, for applied stress amplitudes below 150 MPa, failures have been found below 10^6 cycles and above 5 × 10^6 cycles, depending on the testing method.

The slope of the finite fatigue life range for the conventional and ultrasonic fatigue tests is quite different, and this can indicate a change in the failure mode [56]. It can also be attributed to the different number

Table 5
Fatigue test results for PBF-LB Al2139ZrTi specimens showing applied stress, number of cycles to failure, and critical defect metrics including size and proximity to surface (distance from edge of the defect to surface of the specimen).

Specimen ID	Stress (MPa)	Number of Cycles (N_f)	Defect Size (μm)	Distance from defect to surface (μm)
F1	94	5.00E + 06	–	–
F2	94	5.00E + 06	–	–
F3	117	5.00E + 06	–	–
F4	117	5.00E + 06	–	–
F5	117	1.31E + 06	79.05	0.00
F6	117	2.94E + 05	205.38	0.00
F7	140	1.24E + 05	129.54	0.00
F8	140	1.10E + 05	130.12	5.95
F9	140	4.62E + 04	156.46	0.00
F10	140	3.90E + 04	312.31	3.80
F11	187	1.45E + 05	70.00	0.00
F11	187	1.45E + 05	40.16	0.00
F12	187	8.32E + 04	70.75	0.00
F13	187	5.72E + 04	72.80	0.00
F14	234	6.27E + 04	64.02	0.00
F15	234	2.31E + 04	86.02	0.00
F16	234	2.15E + 04	172.07	3.83
F17	281	3.47E + 04	34.09	28.38
F17	281	3.47E + 04	49.64	0.00
F18	281	2.39E + 04	66.33	0.00
F19	281	7.36E + 03	183.38	107.73
F20	328	3.83E + 03	352.79	151.60
F21	328	2.99E + 03	219.61	92.75
F22	328	2.50E + 03	247.43	0.00
F23	374	4.42E + 03	239.88	946.06
F24	374	3.29E + 03	90.44	0.00
F25	374	2.81E + 03	242.23	347.56

of specimens tested through conventional tests and the ultrasonic fatigue testing equipment. Indeed, size-effect and specimen geometry are not expected to significantly affect the slope of the P-S-N curves. However, it is as if the experimental failures obtained through ultrasonic fatigue tests are shifted upward. This unexpectedly large variability in the fatigue life and dependence on the testing methods can be explained by considering the "strain rate effect", i.e., the variation of the fatigue response with the applied load frequency. However, literature works [57,58] have shown that aluminum alloys, as face-centered cubic (FCC) materials, are not prone to a significant frequency effect when subjected to ultrasonic fatigue tests. Another possible reason is the size effect; in a probabilistic framework, the probability of large defects tends to increase with the loaded volume. Indeed, the tested volume of the two specimen types is quite different, being equal to about 60 mm^3 for the conventional fatigue tests (computed by considering the volume of the specimen part with constant cross-section) and equal to 42 mm^3 (computed as the V_{90} according to Murakami definition, i.e., the volume of material subjected to a stress amplitude above the 90 % of the maximum applied stress). Size-effect can be reliably verified by comparing the characteristic sizes of the defects originating the fatigue failure, i.e., the killer defect $\sqrt{a_c}$ in the two investigated specimen types. The parameter $\sqrt{a_c}$ corresponds to the projected area of the killer defect in a plane perpendicular to the direction of the maximum applied stress [38,39].

Fig. 20 shows the interval data of the $\sqrt{a_c}$ values for the Conventional and Ultrasonic specimens. According to Fig. 20, defects in conventionally tested specimens can be significantly larger than defects in specimens subjected to ultrasonic fatigue tests. This explains why, for the same applied stress amplitude, failures at significantly different numbers of cycles have been experimentally found. Moreover, the variability of $\sqrt{a_c}$ in conventional specimens is higher, explaining why the data are more dispersed in the S-N plot in Fig. 19, with the distance between the 0.9-th curve and the 0.1-th curve larger than that found for the ultrasonic fatigue tests. Together with the size effect, another possible reason for the difference between the $\sqrt{a_c}$ values is the distance of the specimens from the surface of blocks from which they have been cut. Indeed, according to [37], due to their smaller size, hourglass specimens for ultrasonic fatigue tests have been obtained at a larger distance from the block surface, affecting the defect population. Furthermore, the specimen shape also plays a relevant role in the defect population (according to [37], "*It was observed that even just a small alteration in the size or shape of a part made with LB-PBF may have a considerable impact on the formation and distribution of defects*").

Fig. 20 provides relevant information on the killer defect size, but it fails to account for the defect location, which is another important factor in the crack nucleation process. Moreover, Fig. 20 cannot capture the relationship between the applied stress amplitude and the defect size on the fatigue life. For this purpose, the stress intensity factor (SIF) for each killer defect has been computed. According to [59,60], the SIF for a defect, K_d, can be computed according to Eq. (2):

$$K_d = Y \bullet s_a \bullet \sqrt{\pi \bullet \sqrt{a_c}} \tag{2}$$

being s_a the applied stress amplitude and Y a coefficient accounting for

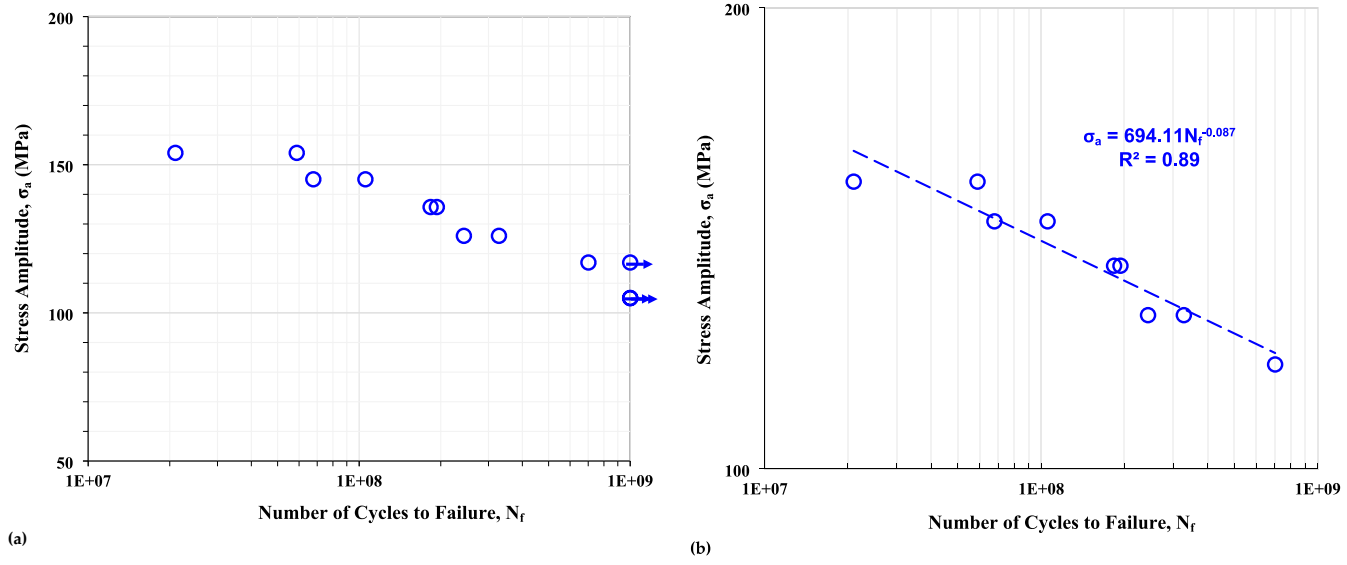

Fig. 16. (a) VHCF S-N data obtained from ultrasonic fatigue testing at 20 kHz, arrows indicating runout samples at 10^9 cycles; (b) Basquin fit of the VHCF data (excluding runouts).

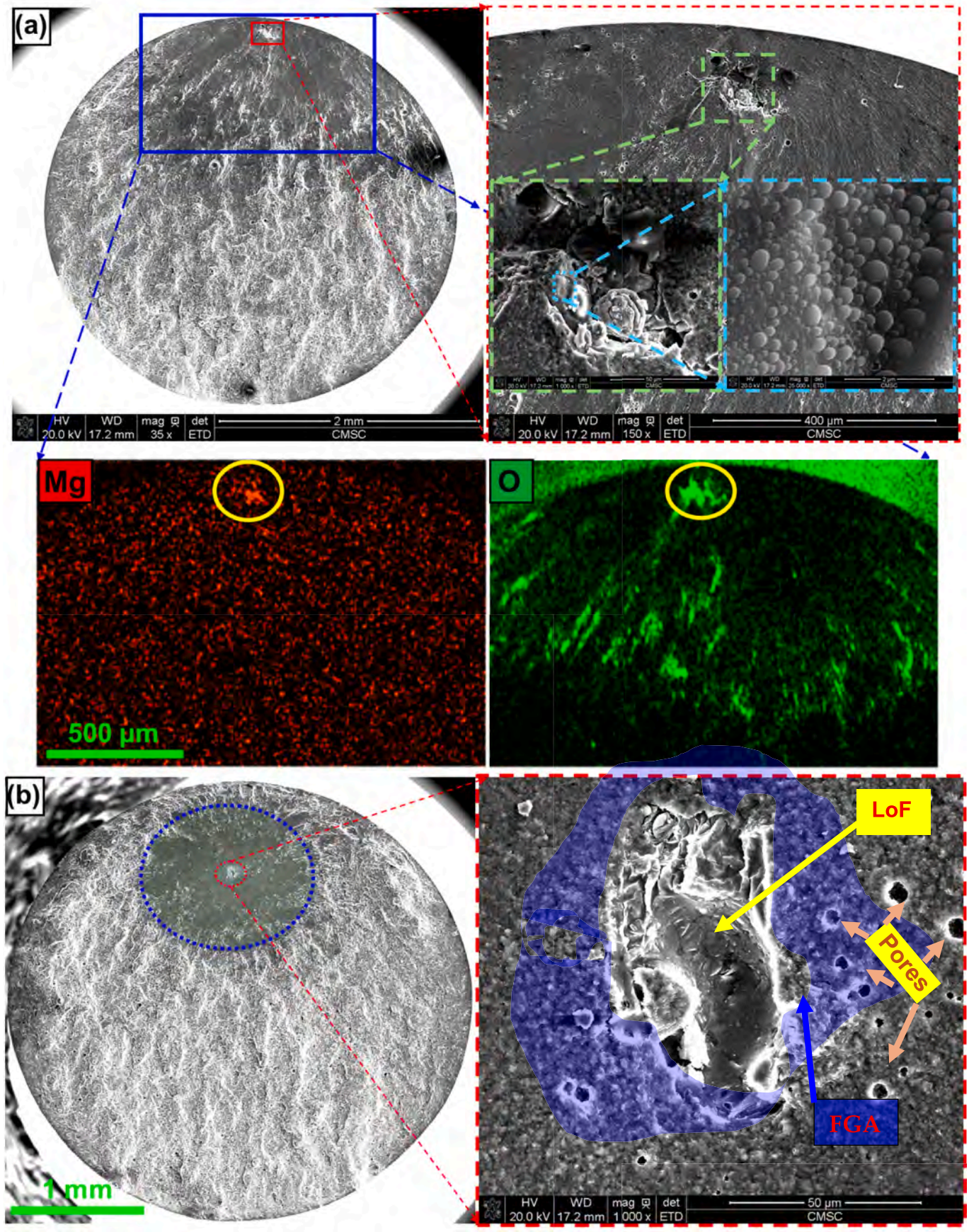

Fig. 17. LoF-initiated VHCF fracture: (a) Specimen U5 (3.28×10^8 cycles at 126 MPa) failed from a near-surface LoF defect with complex shape, un-melted particles, and presence of oxides; (b) Specimen U7 (1.93×10^8 cycles at 136 MPa) shows a deep LoF defect with a distinct fisheye and central fine granular area.

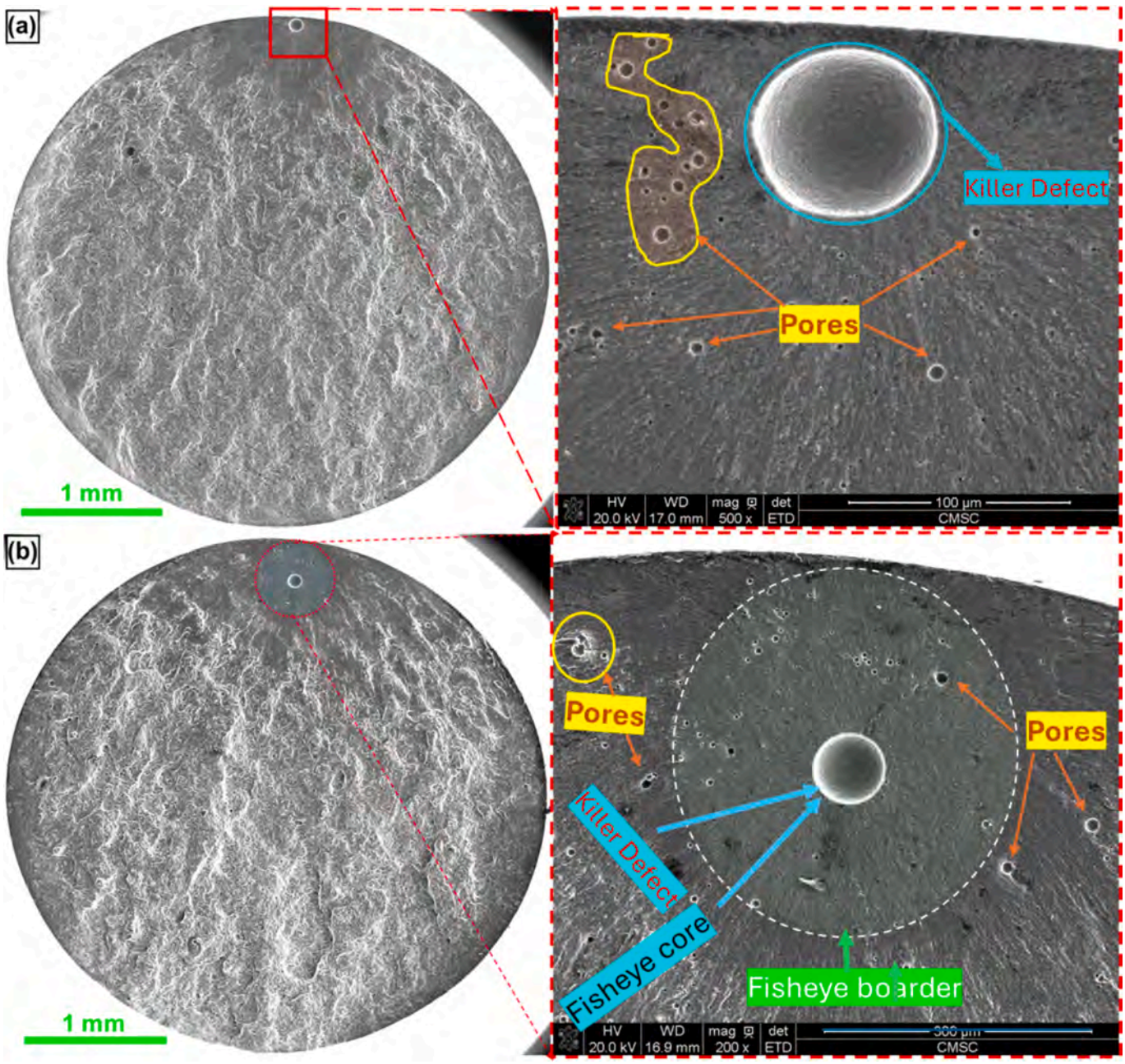

Fig. 18. Spherical-pore-initiated failure: (a) Specimen U8 (1.83×10^8 cycles at 136 MPa) failed from a shallow spherical pore without fisheye formation; (b) Specimen U9 (1.05×10^8 cycles at 145 MPa) failed from a deep internal pore with a distinct fisheye border.

the defect location influence, equal to 0.65 for a surface defect and 0.5 for an internal defect. Accordingly, for the same $\sqrt{a_c}$, a surface defect is characterized by an SIF 1.3 times larger. Fig. 21 plots the SIF for the number of cycles to failure for conventional and ultrasonic specimens.

According to Fig. 21, the SIFs for the conventional tests are larger than the SIFs of specimens subjected to ultrasonic fatigue tests and tend to decrease with the number of cycles to failure. For the specimens that failed below 10^4 cycles, the SIF is above $3\text{MPa}\sqrt{\text{m}}$ – reaching up to $6\text{MPa}\sqrt{\text{m}}$ for the failure below 10^3 cycles, indicating that the fatigue crack has propagated directly from the killer defect. For these specimens, the large applied stress amplitude or defect size (or both) has therefore induced a premature failure and propagation directly from the defect. Larger defects in these specimens were found and explained by considering the size effect, as confirmed through the analysis carried out in Fig. 20. On the other hand, in the VHCF region, the SIFs show a quasi-asymptotic trend, with a slope significantly smaller than that found for specimens subjected to conventional tests, and an average value of $1.1\text{MPa}\sqrt{\text{m}}$. For these failures, a large portion of the fatigue life has been spent in the crack initiation phase in a small region close to the defect, thus explaining the significantly larger fatigue life of these specimens. Accordingly, above 10^6 cycles, a transition in the failure modes can be observed (from “direct propagation from defects” to a “long crack initiation phase and a following propagation”, with the propagation covering a small portion of the fatigue life), which is quite typical for VHCF test results [56]. This trend had not been captured in the S-N plot, due to the possible size effect and influence of the specimen geometry discussed above. The SIF for killer defects found in ultrasonic fatigue tests can be reasonably assumed as the SIF threshold and to be independent from the number of cycles to failure, according to the trend in Fig. 21. The SIF threshold can be moreover assumed normally

Table 6
Summary of fractographic investigations from the VHCF fractured specimens.

ID	Stress (MPa)	Number of Cycles (N_f)	Defect Size (μm)	Defect to surface distance (μm)	$\sqrt{area}$ Fisheye (μm)	Defect Type
U1	105	1.00E + 09	–	–	–	
U2	105	1.00E + 09	–	–	–	
U3	117	1.00E + 09	–	–	–	
U4	117	7.01E + 08	110.25	204.17	533.26	Pore
U5	126	3.28E + 08	91.49	39.26	–	LoF
U6	126	2.43E + 08	96.12	1021.91	1659.33	LoF
U7	136	1.93E + 08	59.05	548.96	910.24	LoF
U8	136	1.83E + 08	71.30	10.62	–	Pore
U9	145	1.05E + 08	71.36	196.59	347.44	Pore
U10	145	6.77E + 07	85.90	1217.60	1638.22	Pore
U11	154	5.88E + 07	53.81	12.73	–	Pore
U12	154	2.10E + 07	99.78	438.88	1049.77	LoF + Pore

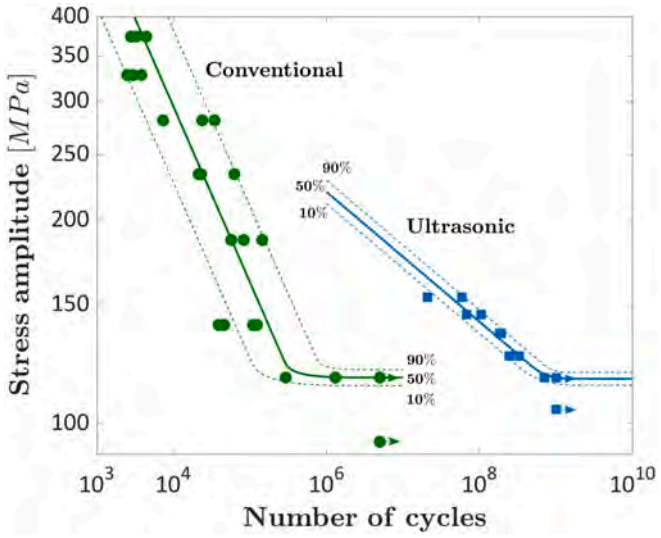

Fig. 19. S-N plot of experimental data and estimated probabilistic S-N curves (0.1-th, 0.5-th, 0.9-th quantiles).

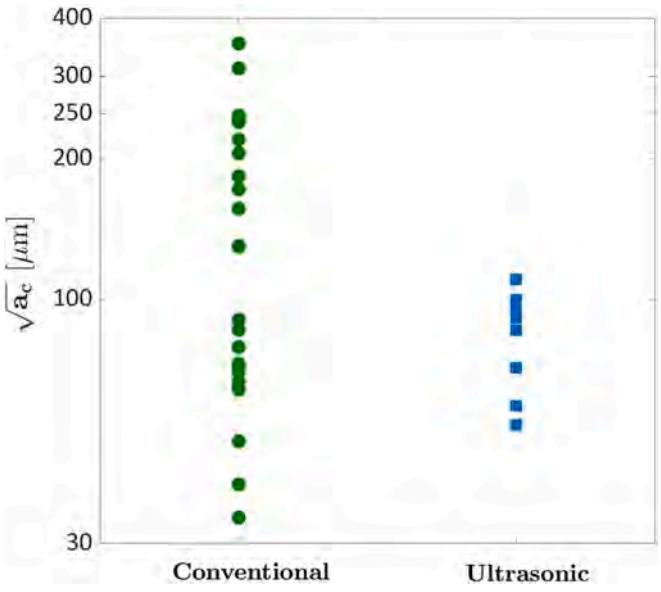

Fig. 20. $\sqrt{a_c}$ of the killer defect for the conventional and ultrasonic fatigue tests.

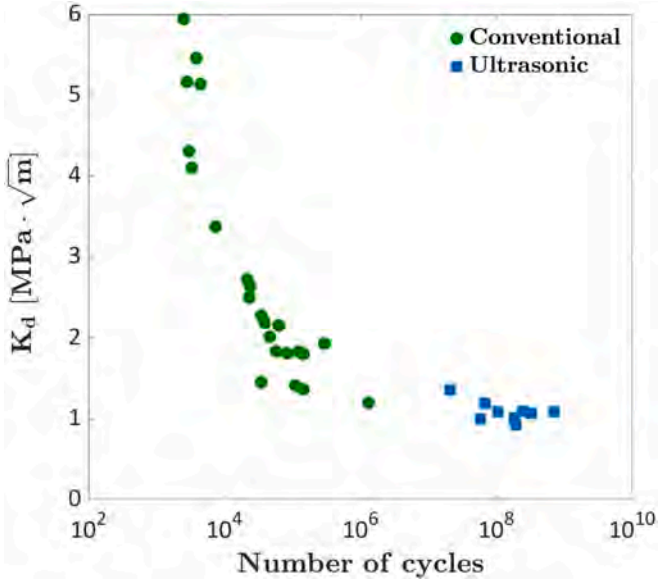

Fig. 21. SIF versus the number of cycles to failure (data from both conventional fatigue, i.e., servo-hydraulic fatigue tester, and VHCF, i.e., ultrasonic fatigue tester is included).

distributed, with the 10th quantile, corresponding to a 90 % reliability and equal to 0.93 MPa$\sqrt{m}$, which can be conservatively assumed as the SIF threshold for a safe design in this ultralong life range. Defects with a SIF value above this threshold are expected to fail in the HCF life range, with a crack propagating directly from a defect. This value aligns closely with values reported for high-strength Al-Mg-Zr alloys in the VHCF domain [51] and is somewhat lower than those reported for TiB_2-reinforced Al-Cu-Mg-Ag alloys processed via PBF-LB [61].

4. Conclusions

Based on the comprehensive investigation of the microstructure, defect characteristics, tensile properties, and fatigue response of a post-aged PBF-LB Al2139ZrTi alloy, the following conclusions are drawn:

I. The alloy exhibited a refined microstructure with uniformly distributed equiaxed grains averaging ~ 1.5 μm with no preferred texture. Precipitation was dominated by thermally stable Al_3(Zr, Ti) dispersoids/plates and Mn-refined intermetallics, Al_7Cu_2 (Fe, Mn), $Al_{20}Cu_2Mn_3$, while conventional Al_2Cu-based Ω and θ′ phases were sparsely distributed. The suppression of Al_2Cu-based precipitates is attributed to solute consumption by dispersoids and Zr/Ti-driven precipitation pathways.
II. The alloy achieved excellent tensile properties in the post-aged condition, with a yield strength of ~ 468 MPa, UTS of ~ 573 MPa, and elongation of ~ 6.5 %. The strengthening results from the synergy between grain refinement, nano-dispersoid hardening, and thermally stable precipitates.
III. Conventional fatigue failures were consistently initiated from LoF defects located at or in the vicinity of the surface. Fractography

revealed both single and multiple initiation zones, often accompanied by un-melted particles and oxide films, indicating that surface accessibility and defect complexity critically governed early crack nucleation and propagation behavior.

IV. In the VHCF regime, failure mechanisms diverged based on defect location. Surface-connected defects, whether LoF or spherical pores, led to early crack initiation without fisheye formation, while deeply embedded defects (>200 μm) exhibited classic VHCF features, including distinct fisheye patterns and FGAs surrounding the initiation site.

V. Analysis of the S-N data across both conventional and VHCF regimes indicates that the endurance limit of the alloy lies just below 117 MPa. Runout was consistently observed at 117 MPa in both regimes, while failures occurred at the same stress level in select specimens, suggesting sensitivity to defect population. The next lower stress levels, 94 MPa in conventional and 105 MPa in VHCF, produced no failures, reinforcing the conclusion that the true endurance limit resides just under 117 MPa. These results support a median fatigue strength of ~ 116 MPa, marking a consistent fatigue threshold across regimes and emphasizing the alloy's promising cyclic durability even beyond 10^9 cycles when near-surface defects are minimized.

VI. The comparable endurance limits and defect variability between conventional and ultrasonic specimens can be attributed to specimen size effects, where larger conventional specimens presented larger killer defects, higher stress intensity factor (K_d), and shorter life, whereas VHCF failures were governed by prolonged initiation near internal flaws. A SIF threshold value of 0.93 MPa$\sqrt{m}$, estimated by considering a 90% reliability level, can be conservatively considered for a safe design of parts subjected to loads for a very high number of cycles.

Together, these findings demonstrate that the rapid solidification of PBF-LB processing, combined with tailored post-aging, yields a refined and stable microstructure with enhanced mechanical properties. Fatigue performance is governed by defect variability. With an effective defect control strategy, PBF-LB Al2139ZrTi demonstrates strong potential for use in fatigue-critical, high-performance structural applications.

CRediT authorship contribution statement

Shawkat I. Shakil: Writing – original draft, Methodology, Investigation, Formal analysis, Data curation. **Wiktor Bednarczyk:** Writing – review & editing, Software, Methodology, Investigation, Formal analysis. **Marta Gajewska:** Writing – review & editing, Visualization, Software, Methodology, Investigation, Data curation. **Zaynab Mahbooba:** Writing – review & editing, Validation, Resources, Project administration. **Ankit Saharan:** Writing – review & editing, Resources, Project administration. **Andrea Tridello:** Writing – review & editing, Software, Methodology, Formal analysis, Data curation. **Alessandro Benelli:** Software, Methodology, Investigation, Data curation. **Meysam Haghshenas:** Writing – review & editing, Supervision, Resources, Project administration, Funding acquisition, Conceptualization.

Declaration of competing interest

The authors declare that they have no known competing financial interests or personal relationships that could have appeared to influence the work reported in this paper.

Data availability

Data will be made available on request.

References

[1] Cho A, Lisagor WB, Bales TT. Development and Processing Improvement of Aerospace Aluminum Alloys-Development of Al-Cu-Mg-Ag Alloy (2139), 2007, NASA/CR-2007-215094, https://ntrs.nasa.gov/citations/20080009425.

[2] Dixit S, Liu S. Laser additive manufacturing of high-strength aluminum alloys: challenges and strategies. J Manuf Mater Proces 2022;6(6):156.

[3] Martin JH, Yahata BD, Hundley JM, Mayer JA, Schaedler TA, Pollock TM. 3D printing of high-strength aluminium alloys. Nature 2017;549(7672):365–9.

[4] Nabavi SF, Dalir H, Farshidianfar A. A comprehensive review of recent advances in laser powder bed fusion characteristics modeling: metallurgical and defects. Int J Adv Manuf Technol 2024;132(5):2233–69.

[5] Abd-Elaziem W, Elkatatny S, Abd-Elaziem A-E, Khedr M, Abd El-baky MA, Hassan MA, et al. On the current research progress of metallic materials fabricated by laser powder bed fusion process: a review. J Mater Res Technol 2022;20:681–707.

[6] Martucci A, Aversa A, Lombardi M. Ongoing challenges of laser-based powder bed fusion processing of Al alloys and potential solutions from the literature—a review. Materials 2023;16(3):1084.

[7] Rometsch PA, Zhu Y, Wu X, Huang A. Review of high-strength aluminium alloys for additive manufacturing by laser powder bed fusion. Mater Des 2022;219:110779.

[8] Chowdhury S, Yadaiah N, Prakash C, Ramakrishna S, Dixit S, Gupta LR, et al. Laser powder bed fusion: a state-of-the-art review of the technology, materials, properties & defects, and numerical modelling. J Mater Res Technol 2022;20:2109–72.

[9] Fiegl T, Franke M, Körner C. Correlation of powder degradation, energy absorption and gas pore formation in laser-based powder bed fusion process of AlSi10Mg0.4. Addit Manuf 2022;56:102917.

[10] Okunkova AA, Shekhtman SR, Metel AS, Suhova NA, Fedorov SV, Volosova MA, et al. On defect minimization caused by oxide phase formation in laser powder bed fusion. Metals 2022;T.

[11] Brice CA, Tayon WA, Newman JA, Kral MV, Bishop C, Sokolova A. Effect of compositional changes on microstructure in additively manufactured aluminum alloy 2139. Mater Charact 2018;143:50–8.

[12] Shakil SI, Bednarczyk W, Gajewska M, Mahbooba Z, Saharan A, Haghshenas M. Metallurgical and tensile properties of a laser powder bed fused scandium-free Al–Mg–Zr Alloy. Mater Chem Phys 2025;335:130542.

[13] Bakavos D, Prangnell PB, Bes B, Eberl F. The effect of silver on microstructural evolution in two 2xxx series Al-alloys with a high Cu: Mg ratio during ageing to a T8 temper. Mater Sci Eng A 2008;491(1–2):214–23.

[14] Cayless RBC. Alloy and temper designation systems for aluminum and aluminum alloys. ASM International; 1990. https://doi.org/10.31399/asm.hb.v02.a0001058.

[15] Brice C, Shenoy R, Kral M, Buchannan K. Precipitation behavior of aluminum alloy 2139 fabricated using additive manufacturing. Mater Sci Eng A 2015;648:9–14.

[16] Shakil SI, Zoeram AS, Pirgazi H, Shalchi-Amirkhiz B, Poorganji B, Mohammadi M, et al. Microstructural-micromechanical correlation in an Al–Cu–Mg–Ag–TiB2 (A205) alloy: additively manufactured and cast. Mater Sci Eng A 2022;832:142453.

[17] Shakil SI, Bednarczyk W, Gajewska M, Mahbooba Z, Saharan A, Tridello A, et al. Fatigue characteristics of a newly developed laser powder bed fused scandium-free Al-Mg-Zr-Mn alloy. Int J Fatigue 2025;193:108738.

[18] Samuel E, Zedan Y, Samuel AM, Samuel FH. An experimental study of the effect of Ag, Cu, Li, Mg, Ni, Ti, Sc, Zr on grain refining in binary and multicomponent Al-based alloys. J Mater Res Technol 2024;30:332–47.

[19] Del Guercio G. Hot cracking elimination strategies in aluminium alloys fabricated by PBF-LB/M. University of Nottingham; 2023. PhD Thesis.

[20] Larini F, Casati R, Marola S, Vedani M. Microstructural evolution of a high-strength Zr-Ti-Modified 2139 aluminum alloy for laser powder bed fusion. Metals 2023;13(5):924.

[21] Nie X, Zhang H, Zhu H, Hu Z, Ke L, Zeng X. Effect of Zr content on formability, microstructure and mechanical properties of selective laser melted Zr modified Al-4.24Cu-1.97Mg-0.56Mn alloys. J Alloy Compd 2018;764:977–86.

[22] Qbau N, Nam ND, Ca NX, Hien NT. The crack healing effect of scandium in aluminum alloys during laser additive manufacturing. J Manuf Process 2020;50:241–6.

[23] Chen Z, Yan K. Grain refinement of commercially pure aluminum with addition of Ti and Zr elements based on crystallography orientation. Sci Rep 2020;10(1):16591.

[24] Elambasseril J, Benoit MJ, Zhu S, Easton MA, Lui E, Brice CA, et al. Effect of process parameters and grain refinement on hot tearing susceptibility of high strength aluminum alloy 2139 in laser powder bed fusion. Prog Addit Manuf 2022;7(5):887–901.

[25] Rees DT, Leung CLA, Elambasseril J, Marussi S, Shah S, Marathe S, et al. In situ X-ray imaging of hot cracking and porosity during LPBF of Al-2139 with TiB2 additions and varied process parameters. Mater Des 2023;231:112031.

[26] The Alumnium Association, International Alloy Designations and Chemical Composition Limits for Wrought Aluminum and, (2015), https://www.aluminum.org/sites/default/files/2021-11/TealSheet.pdf.

[27] EOS Aluminium Al2139 AM Material Data Sheet. https://www.eos.info/metal-solutions/metal-materials/aluminium#eos-aluminium-al2139-am.

[28] ASTM E8/E8M-24, Standard test methods for tension testing of metallic materials, Annual book of ASTM standards, ASTM International, https://store.astm.org/e0008_e0008m-24.html.

[29] ASTM E466-21, Standard practice for conducting force controlled constant amplitude axial fatigue tests of metallic materials, ASTM International, https://store.astm.org/e0466-21.html.

[30] Rouxel B, Ramajayam M, Langan TJ, Lamb J, Sanders PG, Dorin T. Effect of dislocations, Al3(Sc,Zr) distribution and ageing temperature on θ′ precipitation in Al-Cu-(Sc)-(Zr) alloys. Materialia 2020;9:100610.
[31] Deane K, Sanders P. Effect of Zr additions on thermal stability of Al-Cu precipitates in as-cast and cold worked samples. Metals 2018;8(5):331.
[32] Hu K, Zou C, Wang H, Wei Z. Influence of Ti elements on the evolution of microstructure, mechanical properties and thermal stability of Al-Cu alloy. J Alloy Compd 2023;952:169860.
[33] Wang Y, Lin X, Zhao Y, Dong Q, Shi S, Gao X, et al. Microstructure and strengthening mechanisms of Zr-modified Al–Cu–Mg alloy processed by selective laser melting. Mater Sci Eng A 2023;870:144874.
[34] Huang H, Li W, Hu C, Ding L, Jia Z, Zhou N. Dispersoid characteristics and elevated temperature creep resistance of Al–Si–Mg cast alloy with Zr addition. Mater Sci Eng A 2022;836:142570.
[35] Knipling KE, Seidman DN, Dunand DC. Ambient-and high-temperature mechanical properties of isochronally aged Al–0.06 Sc, Al–0.06 Zr and Al–0.06 Sc–0.06 Zr (at. %) alloys. Acta Mater 2011;59(3):943–54.
[36] Worthley B. Equivalent square of rectangular fields. Br J Radiol 1966;39(463):559.
[37] Tahmasbi K, Muhammad M, Avateffazeli M, Yaghoobi M, Tridello A, Paolino DS, et al. Very high cycle fatigue characteristics of laser beam powder bed fused AlSi10Mg: a systematic evaluation of part geometry. Int J Fatigue 2024;189:108544.
[38] Murakami Y. Material defects as the basis of fatigue design. Int J Fatigue 2012;41:2–10.
[39] Murakami Y, Beretta S. Small defects and inhomogeneities in fatigue strength: experiments, models and statistical implications. Extremes 1999;2:123–47.
[40] Zhang H, Zhu H, Nie X, Yin J, Hu Z, Zeng X. Effect of Zirconium addition on crack, microstructure and mechanical behavior of selective laser melted Al-Cu-Mg alloy. Scr Mater 2017;134:6–10.
[41] Zhang J, Gao J, Song B, Zhang L, Han C, Cai C, et al. A novel crack-free Ti-modified Al-Cu-Mg alloy designed for selective laser melting. Addit Manuf 2021;38:101829.
[42] Zuiko I, Kaibyshev R. Aging behavior of an Al–Cu–Mg alloy. J Alloy Compd 2018;759:108–19.
[43] Gairola S, Jayaganthan R. Influence of heat treatment, microstructure evolution, and damage mechanism on high cycle fatigue behaviour of additively manufactured Ti-modified Al 2024 alloy. Mater Charact 2023;203:113047.
[44] Avateffazeli M, Shakil SI, Khan MF, Pirgazi H, Shamsaei N, Haghshenas M. The effect of heat treatment on fatigue response of laser powder bed fused Al-Cu-Mg-Ag-TiB2 (A20X) alloy. Mater Today Commun 2023;35:106009.
[45] Shukla S, Komarasamy M, Mishra RS. Grain size dependence of fatigue properties of friction stir processed ultrafine-grained Al-5024 alloy. Int J Fatigue 2018;109:1–9.
[46] Kermanidis AT, Zervaki AD, Haidemenopoulos GN, Pantelakis SG. Effects of temper condition and corrosion on the fatigue performance of a laser-welded Al–Cu–Mg–Ag (2139) alloy. Mater Des 2010;31(1):42–9.
[47] Köckritz J, Kögler D, Szlosarek R, Langenhan SG, Kröger M. The effect of surface treatment on the fatigue life of aluminium 2139-AM components manufactured additively by PBF-LB/M. Procedia Struct Integrity 2025;68:962–8.
[48] Gazizov M, Kaibyshev R. High cyclic fatigue performance of Al–Cu–Mg–Ag alloy under T6 and T840 conditions. Trans Nonferrous Met Soc Chin 2017;27(6):1215–23.
[49] Djugum R, Lumley RN, Viano DM, Davidson CJ. Enhanced fatigue resistance in a commercial Al-Cu-Mg alloy through underageing. 2nd International Conference on Self Healing Materials. 2009.
[50] Mehide Hasan Tusher M, Ince A. Exploring VHCF response in L-PBF AlSi7Mg Alloy: influence of T6 heat treatment on microstructural characteristics and defect distribution. Int J Fatigue 2024;187:108471.
[51] Shakil SI, Bednarczyk W, Gajewska M, Mahbooba Z, Saharan A, Tridello A, et al. Microstructure and very high cycle fatigue characteristics of powder bed fused – laser beam (PBF-LB) scandium-free Al-Mg-Zr alloy. Mater Sci Eng A 2025;930:148177.
[52] Murakami Y. Metal fatigue: effects of small defects and nonmetallic inclusions. Academic Press; 2019.
[53] Serrano-Munoz I, Buffiere J-Y, Mokso R, Verdu C, Nadot Y. Location, location & size: defects close to surfaces dominate fatigue crack initiation. Sci Rep 2017;7(1):45239.
[54] Tahmasbi K, Yaghoobi M, Shao S, Shamsaei N, Haghshenas M. Simulated effect of defect volume and location on very high cycle fatigue of laser beam powder bed fused AlSi10Mg. Int J Fatigue 2025;197:108926.
[55] Romano S, Brückner-Foit A, Brandão A, Gumpinger J, Ghidini T, Beretta S. Fatigue properties of AlSi10Mg obtained by additive manufacturing: defect-based modelling and prediction of fatigue strength. Eng Fract Mech 2018;187:165–89.
[56] Shiozawa K, Lu L, Ishihara S. S–N curve characteristics and subsurface crack initiation behaviour in ultra-long life fatigue of a high carbon-chromium bearing steel. Fatigue Fract Eng Mater Struct 2001;24(12):781–90.
[57] Stanzl-Tschegg SE, Mayer H. Fatigue and fatigue crack growth of aluminium alloys at very high numbers of cycles. Int J Fatigue 2001;23:231–7.
[58] Awd M, Siddique S, Johannsen J, Emmelmann C, Walther F. Very high-cycle fatigue properties and microstructural damage mechanisms of selective laser melted AlSi10Mg alloy. Int J Fatigue 2019;124:55–69.
[59] Murakami Y, Effects of small defects and nonmetallic inclusions on the fatigue strength of metals, JSME Int J. Ser. 1, Solid mechanics, strength of materials 32(2) (1989) 167-180.
[60] Murakami Y, Kodama S, Konuma S. Quantitative evaluation of effects of non-metallic inclusions on fatigue strength of high strength steels. I: basic fatigue mechanism and evaluation of correlation between the fatigue fracture stress and the size and location of non-metallic inclusions. Int J Fatigue 1989;11(5):291–8.
[61] Avateffazeli M, Shakil SI, Behvar A, Attallah MM, Simsiriwong J, Tridello A, et al. Very high cycle fatigue of laser powder bed fused Al-Cu-Mg-Ag-TiB2 (A20X) Alloy: stress relief and aging treatments. Int J Fatigue 2024;183:108281.